Nano Research

ISSN 1998-0124 CN 11-5974/O4
https://doi.org/10.26599/NR.2026.94909307

Research Article

Modulation of the electronic structure of a single-atom Ni catalyst for sensitive and simultaneous detection of dopamine and hydroquinone

Yanliang Zhai[1], Ying-Jun Wang[2], Xue Lu[1], Qian Wang[1], J. Hugh Horton[5], Yu Wang[4], Ruihan Wu[1], Heyong Huang[3](✉), Zhijun Li[1](✉)

[1] State Key Laboratory of Continental Shale Oil, Joint International Research Laboratory of Advanced Chemical Catalytic Materials & Surface Science, College of Chemistry and Chemical Engineering, Northeast Petroleum University, Daqing 163318, China

[2] College of Chemical Engineering and Technology, Yantai Nanshan University, Yantai 265713, China

[3] School of Environment, Analysis and Testing Center, Nanjing Normal University, Nanjing 210023, China

[4] Jiangsu Collaborative Innovation Centre of Biomedical Functional Materials, School of Chemistry and Materials Science, Nanjing Normal University, Nanjing 210023, China

[5] Department of Chemistry, Queen's University, Kingston K7L 3N6, Canada

Nano Res., **Just Accepted Manuscript** • https://doi.org/10.26599/NR.2026.94909307

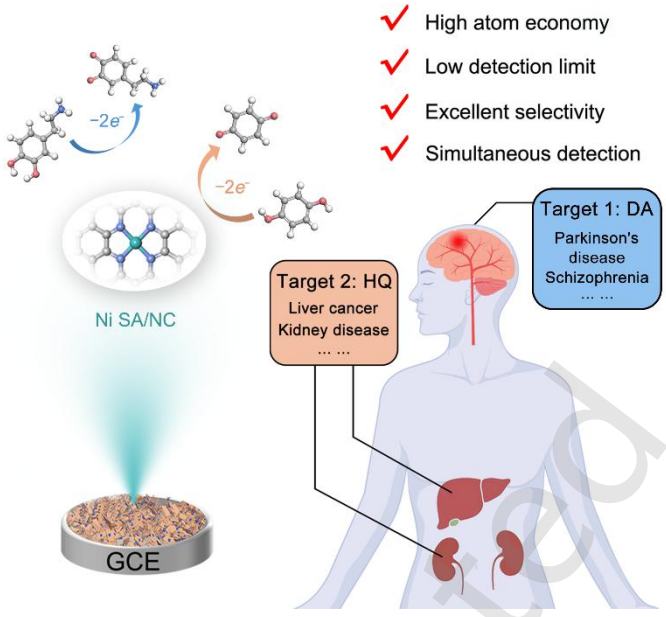
https://www.sciopen.com/journal/1998-0124 on Nov. 2, 2026

© The Authors(s)

Just Accepted

This is a "Just Accepted" manuscript, which has been examined by the peer-review process and has been accepted for publication. A "Just Accepted" manuscript is published online shortly after its acceptance,which is prior to technical editing and formatting and author proofing. Tsinghua University Press (TUP) provides "Just Accepted" as an optional and free service which allows authors to make their results available to the research community as soon as possible after acceptance. After a manuscript has been technically edited and formatted, and the page proofs have been corrected, it will be removed from the "Just Accepted" web site and published officially with volume and article number (e.g., *Nano Research*, **2025**, *18*, 94906990). Please note that technical editing may introduce minor changes to the manuscript text and/or graphics which may affect the content, and all legal disclaimers that apply to the journal pertain. In no event shall TUP be held responsible for errors or consequences arising from the use of any information contained in these "Just Accepted" manuscripts. To cite this anuscript please use its Digital Object Identifier (DOI®),which is identical for all formats of publication.

TABLE OF CONTENTS (TOC)



A Ni single-atom catalyst embedded in nitrogen-doped carbon (denoted as Ni SA/NC) was synthesized. Owing to the unique electronic structure of the Ni–N_4 configuration and the modulated *d*-band center of Ni, the Ni SA/NC electrode enables simultaneous electrochemical detection of dopamine and hydroquinone with effectively eliminated matrix interference.

Just Accepted

Research Article

Modulation of the electronic structure of a single-atom Ni catalyst for sensitive and simultaneous detection of dopamine and hydroquinone

Yanliang Zhai [1], Ying-Jun Wang [2], Xue Lu [1], Qian Wang [1], J. Hugh Horton [5], Yu Wang [4], Ruihan Wu [1], Heyong Huang [3] ✉, Zhijun Li [1] ✉

[1] State Key Laboratory of Continental Shale Oil, Joint International Research Laboratory of Advanced Chemical Catalytic Materials & Surface Science, College of Chemistry and Chemical Engineering, Northeast Petroleum University, Daqing 163318, China
[2] College of Chemical Engineering and Technology, Yantai Nanshan University, Yantai 265713, China
[3] School of Environment, Analysis and Testing Center, Nanjing Normal University, Nanjing 210023, China
[4] Jiangsu Collaborative Innovation Centre of Biomedical Functional Materials, School of Chemistry and Materials Science, Nanjing Normal University, Nanjing 210023, China
[5] Department of Chemistry, Queen's University, Kingston K7L 3N6, Canada

Received: 3 September 2026; **Revised: 20 October 2026**; **Accepted: 2 November 2026**

✉ Address correspondence to Zhijun Li, zhijun.li@queensu.ca; Heyong Huang, hhynjnu@126.com

Cite this article: *Nano Research*, 2027, 20, 94909307 https://doi.org/10.26599/NR.2026.94909307

ABSTRACT: Simultaneous electrochemical detection of dopamine (DA) and hydroquinone (HQ) is clinically significant but challenging because overlapping redox signals obscure detection on conventional sensing materials. Single-atom catalysts (SACs) offer promising adsorption and electron-transfer capabilities; however, limited synthetic control, poor cycling durability, and inevitable signal interference in complex multi-analyte matrices hamper their application. Herein, we report a nickel single-atom catalyst embedded in nitrogen-doped carbon (Ni SA/NC) with a unique electronic structure that enables simultaneous detection of DA and HQ. Benefiting from the unique Ni–N_4 moieties, the oxidation peaks for DA and HQ are well resolved, enabling simultaneous quantification. Notably, the Ni SA/NC achieves ultra-low detection limits (0.0018 μM for DA and 0.0017 μM for HQ), wide segmented linear response windows, and high anti-interference selectivity toward typical coexisting contaminants. Additionally, the Ni SA/NC exhibits outstanding measurement reproducibility, as evidenced by ultra-low relative standard deviations, alongside favorable storage stability. DFT calculations reveal that the Ni–N_4 configuration modulates the Ni *d*-band center to afford moderate *OH adsorption strength, thereby lowering the electro-oxidation barriers. Overall, this work establishes a rational design paradigm for SAC-based electrochemical sensing materials, offering potential for practical implementations in early disease diagnosis.

KEYWORDS: single-atom catalysts, nickel, electrochemical sensing, simultaneous detection, dopamine, hydroquinone

1 Introduction

Dopamine (DA), a key catecholamine neurotransmitter, plays an essential role in regulating the central nervous, renal, and cardiovascular systems [1]. Abnormal dopamine levels are linked to Parkinson's disease, schizophrenia, and anorexia [2]. Furthermore, its concentration in healthy individuals' peripheral fluids ranges from 0.01 to 1 μM, making precise quantification in biological fluids essential for clinical diagnostics [3]. As a phenolic compound, hydroquinone (HQ) is a prevalent environmental pollutant found in industrial wastewater [4]. Its high toxicity poses significant risks to human health [5]. In particular, DA and HQ coexist in biological fluids, such as blood and urine, of occupationally exposed workers and users of HQ-containing cosmetics [6]. As such, developing a sensing material that is capable of simultaneous detection of DA and HQ is of great value for early warning of human health risks [7].

A variety of analytical methods have been established for quantification of HQ and DA, including high-performance liquid chromatography, fluorescence-based assays, and capillary electrophoresis [8, 9]. Although significant advancements in their analytical performance have been made, several drawbacks remain that make facile and accurate detection difficult. In sharp contrast, electrochemical techniques have gained considerable attention for HQ and DA detection due to their distinct advantages, including simple operation, low cost, high sensitivity, portability, and excellent selectivity [10, 11]. Conventional electrode materials for electrochemical sensing primarily include carbon-based materials (glassy carbon, carbon fibers, and graphene), noble metal nanoparticles (Pt, Au, and Ag), transition metal oxides (NiO, Co_3O_4, and MnO_2), and conducting polymers (polyaniline and polypyrrole) [12–14]. However, several limitations remain that limit the sensing performance of these materials.

Carbon-based electrodes typically suffer from sluggish electron transfer kinetics and a limited number of active

Just Accepted

sites, resulting in low sensitivity and poor selectivity toward analytes with similar redox potentials [15–18]. Noble metal nanoparticles, despite their excellent catalytic activity, are hampered by high cost, susceptibility to aggregation, and surface poisoning during repeated use [19, 20]. Transition metal oxides possess low electrical conductivity, which restricts their electrocatalytic performance, while conducting polymers may suffer from poor long-term stability and limited structural tunability [16, 21]. Moreover, most conventional materials lack well-defined atomic-scale active centers, making it difficult to achieve precise control over analyte adsorption and interfacial electron transfer [22]. These drawbacks have motivated research for advanced sensing materials with high catalytic efficiency, structural homogeneity, and tunable electronic properties.

Single-atom catalysts (SACs) represent a burgeoning class of functional nanomaterials for electrochemical sensing and have ignited immense research interest as a new frontier in electrocatalysis [23–28]. Owing to their maximized atom efficiency and structurally uniform active sites with readily modifiable electronic configurations, SACs are particularly advantageous for promoting strong analyte adsorption and rapid interfacial electron transfer [29–34]. For example, an In_1–N–C single-atom catalyst, with an In–N_4 coordination environment, was prepared by high-temperature annealing of an In–MOF precursor [35]. Its enhanced dopamine oxidation activity was found to originate from the favorable OH adsorption on In–N_4 sites and an elevated *s*/*p*-band center. Yao et al. developed carboxylated carbon nanopipette electrodes decorated with single Au atoms, which leverage high atomic utilization and catalytic activity to enhance the sensitivity and accuracy of DA detection [36]. Theoretical calculations reveal that the Au single atoms reduce the kinetic barrier of the rate-determining step during DA oxidation, thereby accounting for the observed catalytic enhancement. These works underscore the potential of SACs as promising alternatives for electrochemical sensing applications. However, SACs are hindered by poor synthetic controllability and insufficient cycling stability. In dual-analyte detection, single atomic sites promote competitive adsorption and suffer from weak anti-interference capability in complex matrices [37]. Furthermore, atomic-scale mechanistic studies are still lacking. Notwithstanding these efforts, the rational design of SACs for simultaneous DA and HQ detection remains unexplored.

In this work, a Ni single-atom catalyst embedded in a nitrogen-doped carbon support (denoted as Ni SA/NC) was synthesized. Benefiting from the precise modulation of the Ni *d*-band center, distinct adsorption configurations toward DA and HQ are achieved. Aberration-corrected high-angle annular dark-field scanning transmission electron microscopy (AC HAADF-STEM) and X-ray absorption fine structure (XAFS) spectroscopy verify the atomic dispersion of Ni species in a Ni–N_4 coordination configuration. The resulting Ni SA/NC exhibits outstanding electrochemical performance for the simultaneous detection of DA and HQ, as evidenced by well-resolved differential pulse voltammetry (DPV) peaks, ultra-low detection limits, broad multi-segment linear ranges, and high selectivity against interfering species. Density functional theory (DFT) calculations further reveal that the modulated *d*-band center of the Ni–N_4 sites optimizes the *OH adsorption energy and lowers the oxidation barriers. As a consequence, the Ni–N_4 sites facilitate sensitive and simultaneous detection in complex matrices. Collectively, this work establishes a well-defined rational design strategy for single-atom-based electrochemical sensing materials, holding great promise for practical applications in early disease diagnostics.

2 Experimental

2.1 Synthesis of Ni-MOF-74

In a typical synthesis, 0.2120 g of nickel nitrate hexahydrate, 1.302 g of zinc nitrate hexahydrate, and 0.3566 g of 2,5-dihydroxyterephthalic acid were introduced into a solution (60 mL) of water, ethanol, and N, N-dimethylformamide with a volume ratio of 1:1:1. After being sonicated for 30 min, the solution was transferred into a Teflon-lined autoclave and heated at 120 °C for 24 h. The precipitate obtained was washed with ethanol and vacuum-dried at 80 °C to yield Ni-MOF-74 nanocrystals.

2.2 Synthesis of Ni-MOF-74@PDA

In a typical synthesis, 0.2 g of Ni-MOF-74 nanocrystals were dispersed in 20 mL of methanol. Then, 10 mL of methanol solution containing 0.06 g dopamine hydrochloride (pH 8.5) was added dropwise under sonication. The mixture was stirred for 12 h at room temperature before being washed with methanol and dried under vacuum. Finally, Ni-MOF-74@PDA was obtained.

2.3 Synthesis of Ni NPs/NC

In a typical synthesis, the as-obtained Ni-MOF-74@PDA was calcined in an argon atmosphere at 950 °C for 3 h with a ramp rate of 5 °C min^{-1}. This was followed by a second thermal treatment under an NH_3/Ar (v/v=5/95) mixed gas atmosphere at 550 °C for 1 h. The resulting precipitates were denoted as Ni NPs/NC. The Ni loading in Ni NPs/NC was determined to be 3.67 wt.% by ICP-OES.

2.4 Synthesis of Ni SA/NC

In a typical synthesis, the resulting Ni NPs/NC was acid-treated with 10 mL of 2 M sulfuric acid at 100 °C for 24 h before being washed with deionized water and vacuum-dried. The obtained black powder was denoted as Ni SA/NC. The Ni loading in Ni SA/NC was determined to be 0.63 wt.% by ICP-OES.

2.5 Synthesis of NC

NC was prepared via the same method as Ni SA/NC, except that nickel nitrate hexahydrate was omitted.

2.6 Synthesis of Co SA/NC

Co SA/NC was prepared via the same method as Ni SA/NC, except that nickel nitrate hexahydrate was replaced with 0.2197 g of cobalt nitrate hexahydrate. The Co loading in Co SA/NC was determined to be 0.76 wt.% by ICP-OES.

3 Results and Discussion

3.1 Synthesis and characterization of Ni single-atom catalyst

The synthetic procedure for the Ni single atoms embedded in nitrogen-doped carbon (denoted as Ni SA/NC) is illustrated in Fig. 1(a). First, nickel nitrate hexahydrate, zinc nitrate

In Accepted

hexahydrate, and 2,5-dihydroxyterephthalic acid were employed in a self-assembly process to prepare Ni-MOF-74 nanocrystals, as verified by powder X-ray diffraction (XRD) analysis (Fig. S1 in the Electronic Supplementary Material (ESM)). Fourier-transform infrared (FT-IR) spectrum of Ni-MOF-74 reveals prominent peaks at 1568 and 1408 cm^{-1} corresponding to asymmetric and symmetric stretching modes of carboxylate groups (Fig. S2 in the ESM) [38, 39]. As shown in Fig. S3 in the ESM, the scanning electron microscopy (SEM) imaging indicates that Ni-MOF-74 possesses a flower-like structure, formed by the intergrowth of small polyhedral crystals. Subsequently, a polydopamine (PDA) layer was uniformly coated onto the Ni-MOF-74 surface to form a Ni-MOF-74@PDA precursor. This precursor was then subjected to a high-temperature thermal treatment under an argon atmosphere, followed by nitrogen infiltration via annealing in an NH_3 atmosphere, yielding Ni nanoparticles supported on nitrogen-doped carbon (Ni NPs/NC), as shown in Figs. S4 and S5 in the ESM. In this approach, Zn served to spatially isolate Ni atoms during MOF synthesis. Upon pyrolysis, Zn was evaporated, generating a porous structure in the resulting carbon matrix. Finally, the as-obtained Ni NPs/NC was treated with acid to afford the target Ni SA/NC catalyst. The control sample of NC was synthesized and characterized by transmission electron microscopy (TEM); details of which are found in Figs. S6 and S7 in the ESM. To benchmark the sensing performance of Ni SA/NC, a cobalt-based single-atom catalyst (Co SA/NC) was constructed as a control sample, with the corresponding characterizations presented in Figs. S8–S11 in the ESM.

As shown in Figs. 1(b) and 1(c), the SEM images reveal that Ni SA/NC exhibits a crumpled N-doped carbon framework with abundant voids and hierarchical pores, which arise from the collapse of the Ni-MOF-74 precursor. HR-TEM analysis (Fig. 1(d)) shows the absence of discernible metallic nanoparticles or clusters in Ni SA/NC. The selected area electron diffraction (SAED) pattern exhibits characteristics of amorphous carbon, with no detectable diffraction spots corresponding to crystalline Ni phases. Notably, the isolated Ni species were verified by AC HAADF-STEM. Low-magnification AC HAADF-STEM imaging (Fig. 1(e)) demonstrates the successful removal of aggregated Ni species by the acid etching, with no evidence of the presence of metallic Ni nanoparticles. High-magnification AC HAADF-STEM (Fig. 1(f)) shows clearly resolved isolated bright features corresponding to individual Ni atoms (highlighted by yellow circles). The atomic intensity line-scanning profiles

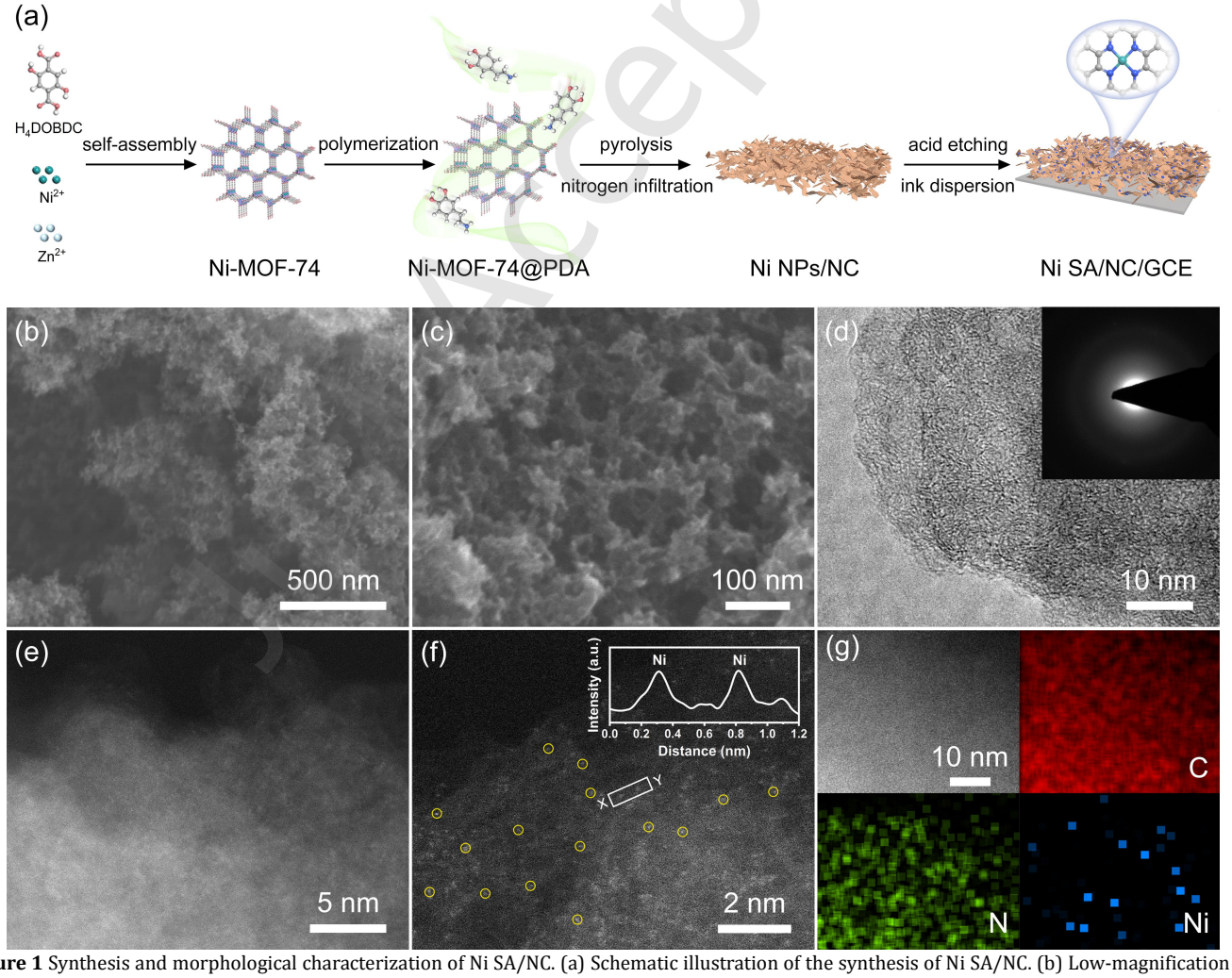


Figure 1 Synthesis and morphological characterization of Ni SA/NC. (a) Schematic illustration of the synthesis of Ni SA/NC. (b) Low-magnification and (c) high-magnification SEM images. (d) HR-TEM image and SAED pattern (inset). (e) Low-magnification AC HAADF-STEM image. (f) High-magnification AC HAADF-STEM image and corresponding intensity profile along the rectangles. (g) EDX elemental mappings.

along the white rectangles (right panel of Fig. 1(f)) further confirm the isolated distribution of Ni atoms. Energy-

dispersive X-ray spectroscopy (EDX) elemental mapping (Fig. 1(g)) corroborated the homogeneous distribution of Ni, N, and C elements throughout the carbon matrix. Together, these morphological characterizations confirm the successful synthesis of Ni SA/NC, featuring atomically dispersed Ni species on the NC support. XRD patterns of samples (Fig. S12 in the ESM) show characteristic peaks of the carbon matrix. The Ni NPs/NC exhibits characteristic diffraction peaks of Ni nanoparticles (PDF#04-0850). Notably, no metallic Ni peaks are observed for Ni SA/NC, confirming the absence of Ni clusters and nanoparticles. In comparison with NC, negligible differences can be observed in the FT- IR spectra of Ni SA/NC and Ni NPs/NC (Fig. S13 in the ESM). Raman spectroscopy was also performed, and the I_{D1}/I_G ratio of Ni SA/NC (1.71) demonstrates a higher number of defects relative to other samples (Fig. S14 in the ESM). This might facilitate the adsorption and activation of the reactant.

The chemical composition and electronic states of the as-prepared catalysts were investigated by X-ray photoelectron spectroscopy (XPS). The survey scan spectra of Ni SA/NC and Ni NPs/NC confirm the presence of Ni, N, C, and O elements (Figs. S15 and S16 in the ESM). The Ni 2*p* XPS spectra (Fig. 2(a)) of Ni SA/NC exhibit a positive shift in binding energy compared to that of Ni NPs/NC, suggesting a higher oxidation state of Ni in Ni SA/NC. This implies the unique electronic metal-support interaction that stems from the electron transfer between the nitrogen-doped carbon support and isolated Ni atoms. To gain deeper insight into the surface chemical states, synchrotron radiation-based photoemission spectroscopy (SRPES) was further conducted to probe the C and N species with enhanced surface sensitivity. As shown in Fig. S17 in the ESM, SRPES C 1*s* spectra are deconvoluted into sp^2 C, sp^3 C, C–N, and O–C=O species [40, 41]. Notably, the Ni SA/NC shows a higher sp^3 C/sp^2 C value of 0.89 than those of Ni NPs/NC (0.79) and NC (0.72). This observation suggests that Ni SA/NC possesses a higher density of structural defects,

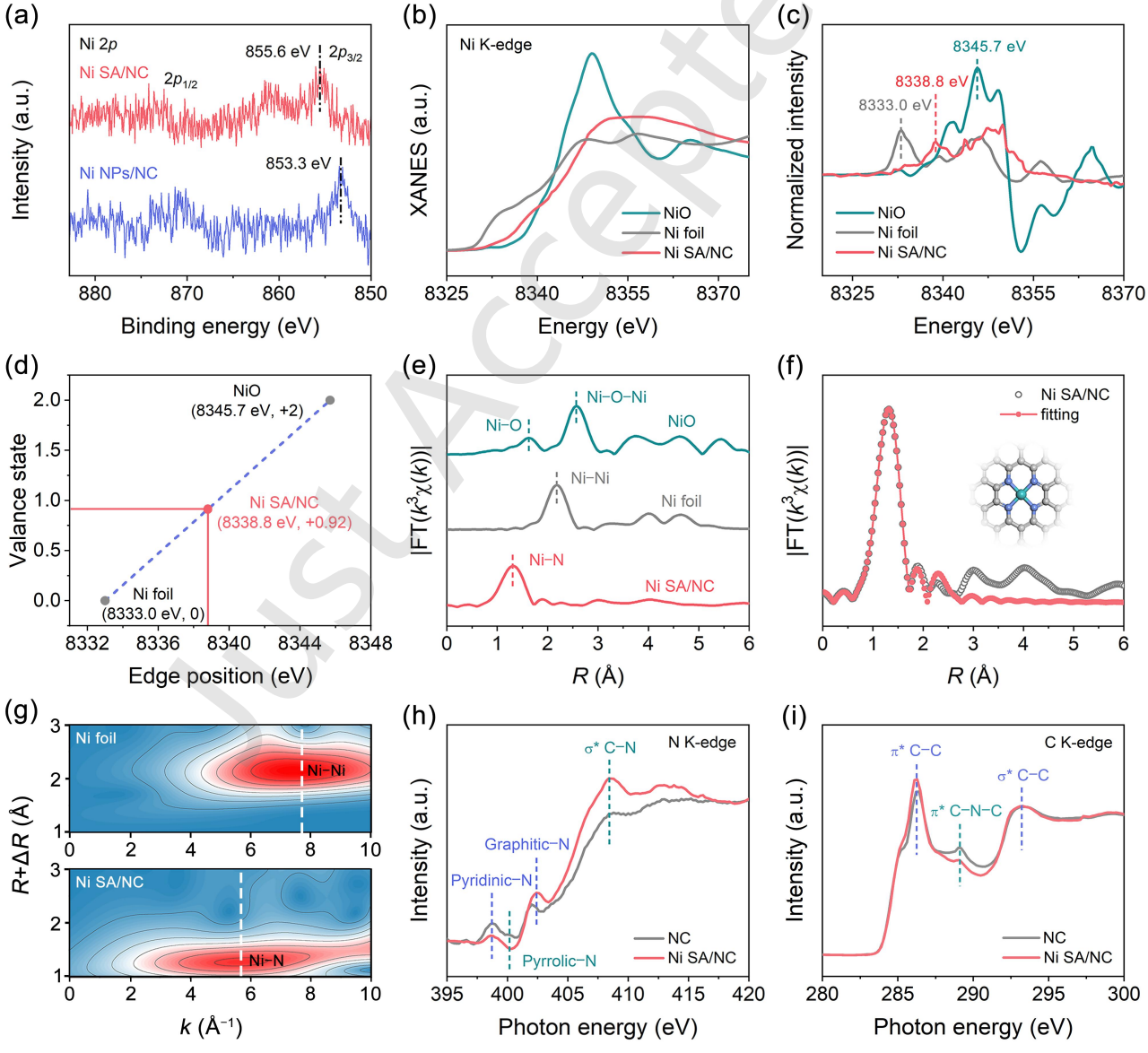


Figure 2 Atomic structural characterizations of Ni SA/NC. (a) XPS Ni 2*p* spectra. (b) Ni K-edge XANES spectra. (c) First-derivative Ni K-edge XANES curves. (d) Correlation between the Ni oxidation states and the energy position of XANES spectra. (e) FT k^3-weighted Ni K-edge EXAFS spectra. (f) Ni K-edge EXAFS fitting results in R space. (g) WT contour plots. (h) N K-edge XANES spectra. (i) C K-edge XANES spectra.

Just Accepted

which is attributable to the incorporation of Ni single atoms into the NC support. The SRPES N 1*s* spectrum (Fig. S18 in the ESM) of Ni SA/NC unveils four types of N species, being pyridinic N, metal–N, pyrrolic N, and graphitic N, respectively [42, 43]. As summarized in Table S1 in the ESM, the Ni SA/NC possesses a higher number of pyridinic N than that of Ni NPs/NC, along with a metal–N ratio of 13.31%. Particularly, the positive shift in pyridinic N binding energy indicates a decrease in electron density around the N atoms, which is consistent with the formation of Ni–N coordination bonds wherein electron density is transferred from the N lone pairs to the d orbitals of Ni.

To gain atomic-level insight into the coordination environment of the Ni centers, XAFS measurements were carried out on Ni SA/NC. As presented in Fig. 2(b), the Ni K-edge X-ray absorption near-edge structure (XANES) spectrum for Ni SA/NC exhibits a near-edge absorption energy positioned between that of Ni foil and NiO. This is suggestive of an oxidation state between Ni^0 and Ni^{2+}. The first-derivative XANES curves (Fig. 2(c)) further corroborate this unique oxidation state. Quantitative analysis of the absorption edge energy (Fig. 2(d)) demonstrates a linear correlation between the oxidation state and energy position, yielding an oxidation state of +0.92 for Ni in Ni SA/NC. The extended X-ray absorption fine structure (EXAFS) provides evidence for the atomic dispersion of Ni. The Fourier-transformed (FT) k^3-weighted EXAFS spectrum (Fig. 2(e)) for Ni SA/NC displays a predominant peak at ~ 1.3 Å, attributable to the Ni–N scattering path. Notably, no peaks are observed for Ni–Ni coordination at ~ 2.2 Å, verifying the absence of metallic Ni clusters or nanoparticles. The quantitative structural parameters of Ni in Ni SA/NC were obtained by least-squares fitting of the EXAFS spectra (Fig. 2(f), Figs. S19 and S20, and Table S2 in the ESM). The fitting results reveal that Ni SA/NC possesses a $Ni–N_4$ coordination configuration, along with a coordination number of 3.8 for the Ni–N scattering path and a bond length of 1.98 Å for Ni–N. The wavelet transform (WT) analysis (Fig. 2(g) and Fig. S21 in the ESM) corroborates the FT-EXAFS findings, revealing a single Ni–N scattering maximum for Ni SA/NC, whereas both Ni foil and NiO show additional features characteristic of Ni–Ni and Ni–O–Ni coordination, respectively. This further confirms the absence of Ni clusters or nanoparticles in Ni SA/NC. Taken together, these results unambiguously establish that Ni SA/NC features atomically dispersed Ni atoms coordinated in a $Ni–N_4$ motif over the NC support.

Soft XANES measurements can reveal the orbital hybridization and charge transfer effects between metal and NC support induced by metal doping [44]. The N K-edge XANES spectra (Fig. 2(h)) reveal four components, corresponding to pyridinic–N, pyrrolic–N, graphitic–N, and σ* C–N resonance [45]. Compared with those of NC, all peaks in Ni SA/NC shift to higher photon energies, accompanied by a marked decrease in pyridinic–N intensity and significant increases in graphitic–N and σ* C–N intensities. These observations suggest electron transfer between NC support upon Ni anchoring, as well as the formation of Ni–pyridinic N sites. The C K-edge XANES spectra (Fig. 2(i)) display three characteristic peaks of π* C–C, σ* C–C, and π* C–N–C [46]. Upon Ni incorporation, the Ni SA/NC sample shows an increased intensity of the π* C–C peak, accompanied by a concomitant decrease in the π* C–N–C peak intensity relative to NC. Again, these changes are attributable to the altered electron density of the NC support upon the anchoring of atomically dispersed Ni atoms. The electronic structures of Ni SA/NC and Ni NPs/NC were probed by synchrotron-based ultraviolet photoelectron spectroscopy (UPS). The valence band maxima (VBM) of Ni SA/NC and Ni NPs/NC are 2.44 and 2.39 eV (Fig. S22 in the ESM), respectively, indicating a slightly higher VBM energy for Ni SA/NC relative to that of Ni NPs/NC. Additionally, the work function (ϕ) values derived from the UPS spectra (Fig. S23 in the ESM) are 4.14 eV for Ni SA/NC and 4.21 eV for Ni NPs/NC, implying a reduced surface barrier and potentially enhanced interfacial charge transfer for small-molecule activation over Ni SA/NC.

3.2 Electrochemical responses of Ni SA/NC for simultaneous detection of dopamine and hydroquinone

The electrochemical sensing performance of Ni SA/NC toward the simultaneous detection of DA and HQ was evaluated. For comparison, Ni NPs/NC and NC were used as controls under identical conditions. Fig. 3(a) compares the differential pulse voltammetry (DPV) current responses of glassy carbon electrodes (GCE) modified with Ni SA/NC, Ni NPs/NC, NC, and Co SA/NC for simultaneous detection of 0.05 μM DA and 0.05 μM HQ in 0.01 M PBS (pH 7.4). The Ni SA/NC sample exhibits substantially higher DPV responses for both DA and HQ compared with Ni NPs/NC, NC, and Co SA/NC (Fig. 3(a) and Table S3 in the ESM). Specifically, the DPV signals of Ni SA/NC are 1.85-, 3.66-, and 2.11-fold higher than those of Ni NPs/NC, NC, and Co SA/NC for DA, and 1.66-, 2.52-, and 1.86-fold higher for HQ, respectively. This highlights the important role of $Ni-N_4$ sites in sensing. The electrochemical charge transfer resistance of samples was studied by electrochemical impedance spectroscopy (EIS). An equivalent circuit model was employed (Fig. S24 in the ESM), and the detailed fitting parameters are listed in Table S4 in the ESM. The charge transfer resistance (R_{ct}) of the Ni SA/NC-modified electrode (128 Ω) is substantially smaller than those of Ni NPs/NC (1228 Ω), NC (1540 Ω), and bare GCE (2501 Ω), indicating the fastest interfacial electron-transfer kinetics. These findings demonstrate that the Ni SA/NC-modified electrode exhibits the highest electrocatalytic activity toward both DA and HQ.

Fig. 3(b) displays the DPV responses of Ni SA/NC under different testing conditions. In the blank 0.01 M PBS (pH 7.4), no discernible oxidation peaks are observed. Upon addition of 0.05 μM DA, a well-defined oxidation peak appears at ~ 0.21 V. Similarly, addition of 0.05 μM HQ alone gives an oxidation peak at ~ 0.06 V. Notably, in the mixed solution containing both DA and HQ (0.05 μM each), the DPV profile displays two well-resolved oxidation peaks at 0.23 V and 0.05 V, respectively, attributed to the electrochemical oxidation of DA and HQ. The effect of pH on the electrochemical responses of DA and HQ on Ni SA/NC was investigated in 0.01 M PBS (pH varies from 5.0 to 8.0), as displayed in Fig. 3(c). To be noted, a progressive negative shift in the oxidation peak potentials of both DA and HQ was observed as the pH increased, suggesting that proton transfer is directly coupled to the electro-oxidation reactions [47]. At pH 7.4, both analytes show strong current responses

Unreviewed

with well-resolved peak separation. Furthermore, the oxidation peak potential of DA and HQ

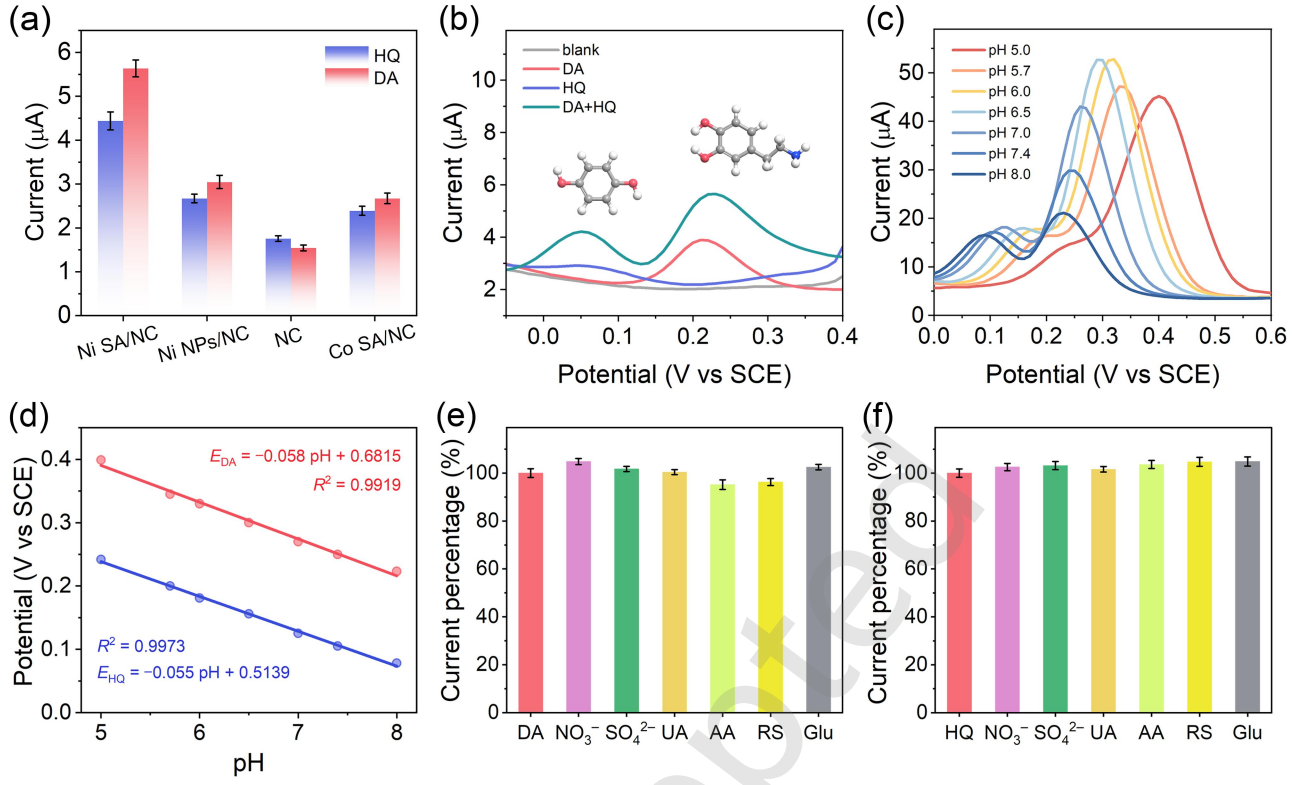


Figure 3 Electrochemical sensing performance of Ni SA/NC toward DA and HQ. (a) DPV responses toward simultaneous detection of DA and HQ. (b) DPV responses of Ni SA/NC for blank electrolyte, individual DA, individual HQ, and a binary mixture of the two. (c) DPV responses of Ni SA/NC toward simultaneous detection of DA and HQ at different pH. (d) Corresponding linear calibration curves of peak potential versus pH value. Anti-interference tests of Ni SA/NC for (e) 1 μM DA and (f) 1 μM HQ detection upon addition of 500 μM interfering substances in 0.01 M PBS (pH 7.4).

shows a linear dependence with solution pH (Fig. 3(d)), with slopes of −58 mV·pH^{-1} and −55 mV·pH^{-1}, respectively. The slopes derived from the pH dependence closely match the theoretical Nernstian slope of −59 mV·pH^{-1}, unequivocally demonstrating that two protons and two electrons are involved in the reversible redox transformations of both analytes [48, 49].

Anti-interference capability is a pivotal criterion in the development of high-performance sensing materials. To assess this property, sequential injections of 500 μM potential interferents, including NO_3^-, SO_4^{2-}, uric acid (UA), ascorbic acid (AA), glucose (Glu), and resorcinol (RS) were carried out in 0.01 M PBS (pH 7.4) containing 1 μM DA at 0.23 V (Fig. 3(e)). Throughout the successive additions, the amperometric response of the Ni SA/NC electrode toward DA exhibits limited changes. In a parallel experiment conducted at 0.05 V in the same electrolyte solution with 1 μM HQ as the target analyte, the identical set of interferents was introduced sequentially (Fig. 3(f)). Likewise, no appreciable fluctuations in the current signals for HQ were observed. Selectivity of Ni SA/NC for the detection of DA and HQ is presented in Fig. S25 in the ESM. The current responses of Ni SA/NC toward DA and HQ are significantly higher than those of interfering species (NO_3^-, SO_4^{2-}, UA, AA, RS, and Glu), demonstrating the exceptional selectivity for DA and HQ. Collectively, these results attest to the high anti-interference performance of Ni SA/NC, highlighting its promising selectivity and reliability for practical electroanalytical applications.

To further evaluate the detection independence of DA and HQ in mixed solutions, the concentration of one analyte was varied while the other was held constant (Figs. 4(a) and 4(b)), and both concentrations were also simultaneously adjusted (Fig. 4(c)). As shown in Fig. 4(a), the peak currents increase progressively with increasing DA concentrations in the presence of 0.05 μM HQ, exhibiting a linear relationship (R^2 = 0.9903) and a sensitivity of 335.32 μA·μM^{-1}·cm^{-2} (Fig. 4(d)). Similarly, enhancing HQ concentrations in the presence of 0.05 μM DA yields a linear response (R^2 = 0.9909) with a sensitivity of 265.24 μA·μM^{-1}·cm^{-2} (Figs. 4(b) and 4(e)). These results confirm that neither analyte interferes with the detection of the other, demonstrating the excellent selectivity and mutual independence of the Ni SA/NC sensing platform. As the concentrations of DA and HQ were simultaneously increased from 0.005 to 0.1 μM, two well-resolved oxidation peaks were consistently observed, with the peak currents of both analytes increasing proportionally (Fig. 4(c)). Furthermore, the calibration plots (Fig. 4(f)) exhibit good linear relationships between peak currents and concentrations for both DA (R^2 = 0.9902) and HQ (R^2 = 0.9924), with sensitivities of 273.10 and 152.46 μA·μM^{-1}·cm^{-2}, respectively. The excellent linearity and negligible cross-interference demonstrate that the Ni SA/NC enables reliable simultaneous detection of DA and HQ in complex matrices.

The analytical performance of the Ni SA/NC modified electrode was further assessed by evaluating the linear calibration ranges and detection limits for DA and HQ. Fig. S26 in the ESM displays the DPV responses of Ni SA/NC toward varying concentrations of DA. We observe that there is a linear relationship between the peak currents and the

Not Accepted

concentrations of DA, and there are three linear intervals (0.007–0.135 μM, 0.135–10.7 μM, and 10.7–1800 μM) with

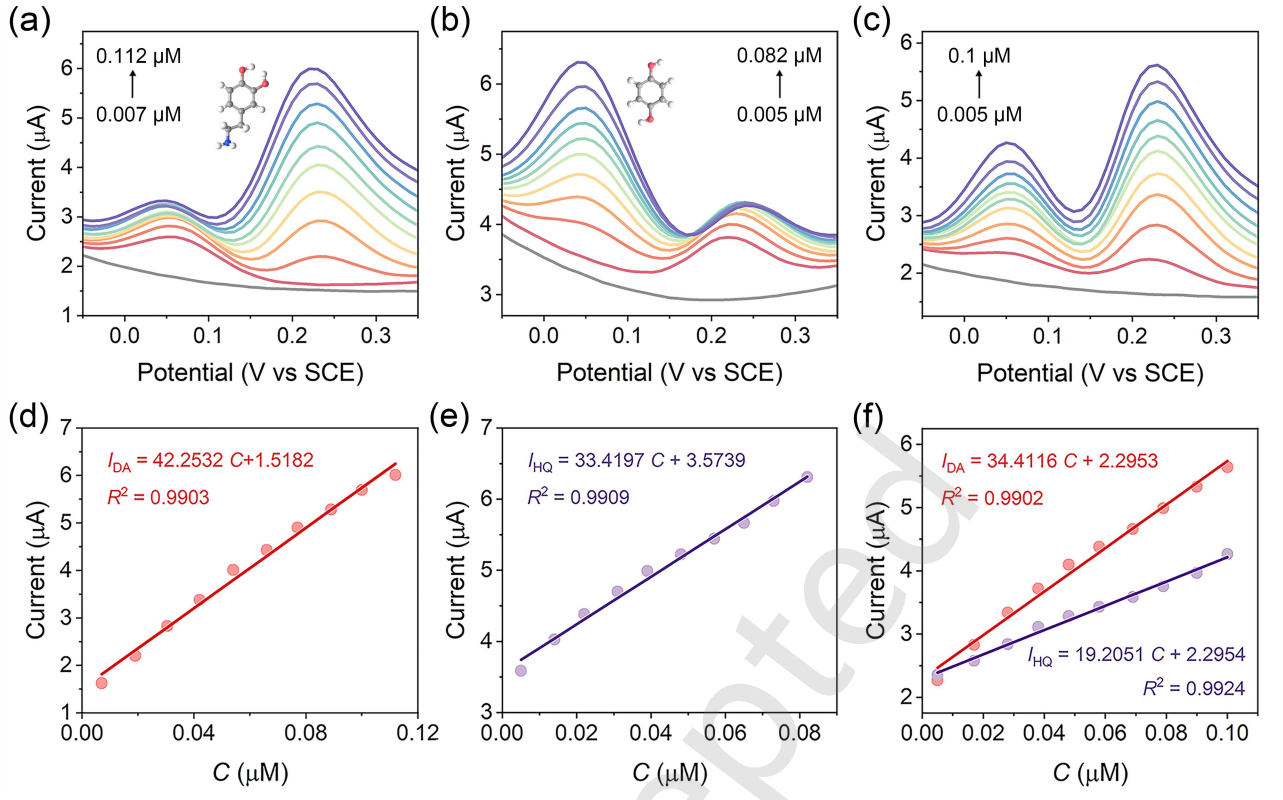


Figure 4 DPV responses of Ni SA/NC in 0.01 M PBS (pH 7.4) at different concentrations. (a) DPV responses of fixed 0.05 μM HQ with different DA concentrations. (b) DPV responses of fixed 0.05 μM DA with different HQ concentrations. (c) DPV responses for synchronous variation of DA and HQ. ((d)–(f)) Corresponding linear calibration plots of the peak currents versus analyte concentrations.

different sensitivities of 165.48, 1.67, and 0.039 $\mu A \cdot \mu M^{-1} \cdot cm^{-2}$, respectively. The observed linear correlation is consistent with a diffusion-limited electrochemical reaction at the Ni SA/NC-modified electrode. Furthermore, the limit of detection (LOD) for DA was 0.0018 μM (S/N = 3). Similarly, a strong linear relationship between the peak currents and concentrations of HQ was evidenced (Fig. S27 in the ESM), and there are three linear intervals (0.005–0.133 μM, 0.133–20 μM, and 20–74 μM) with different sensitivities of 88.17, 2.30, and 0.95 $\mu A \cdot \mu M^{-1} \cdot cm^{-2}$, respectively. Particularly, the LOD for HQ was 0.0017 μM (S/N = 3). It is worth noting that Ni SA/NC shows enhanced performance compared to most of the reported sensing materials in terms of LODs and linear ranges for DA and HQ detection (Tables S6 and S7 in the ESM). This unique combination of high sensitivity at trace levels and a broader quantification window makes Ni SA/NC a promising sensing material for simultaneous detection of DA and HQ.

To probe the electrochemical kinetics governing DA and HQ oxidation at the Ni SA/NC electrode, we performed cyclic voltammetry (CV) measurements. Fig. 5(a) displays the CV curves of the Ni SA/NC electrode in 0.01 M PBS containing 0.05 μM DA. The redox peak currents enhanced with increasing scan rate, which is characteristic of a quasi-reversible electrochemical process [50]. As shown in Fig. 5(b), the redox peak currents are linearly proportional to the square root of the scan rate. Likewise, the CV behavior of Ni SA/NC in the presence of 0.05 μM HQ at different scan rates is presented in Fig. 5(c), which also reveals quasi-reversible redox characteristics. The corresponding linear fitting of peak currents versus $v^{1/2}$ is depicted in Fig. 5(d). The linear relationships are indicative of diffusion-controlled kinetics for the electro-oxidation of DA and HQ at the Ni SA/NC electrode. Coupled with the pH dependence of the peak potentials, the above experimental findings point to a quasi-reversible redox pathway involving two protons and two electrons. Diffusion-controlled analyte mass transport as the rate-determining step ensures a robust linear current-concentration correlation, favoring quantitative applications.

The reproducibility and storage stability of the Ni SA/NC-based electrode were assessed to evaluate its practical applicability. Fig. S28 in the ESM displays the DPV responses of six consecutive measurements at the Ni SA/NC-modified electrode in 0.01 M PBS (pH 7.4) containing 0.05 μM DA and 0.05 μM HQ. The relative standard deviations (RSD) for current fluctuations across the six cycles are below 5%, indicating that Ni SA/NC possesses excellent reproducibility. For independent electrode batches (Fig. S29 in the ESM), the current values of six independent electrodes fluctuated within the range of 96.3% ~ 104.5% for both DA and HQ, and the RSDs were 2.40% and 3.09%, respectively, demonstrating good batch-to-batch reproducibility. To evaluate the anti-fouling performance, the Ni SA/NC electrode was immersed in 10-fold diluted human serum for 4 h, followed by testing the DPV responses to 0.05 μM DA and HQ. The results (Fig. S30 in the ESM) show that after fouling, the current retention rates for DA and HQ were 90.68% and 91.14%, respectively, indicating good anti-fouling capability. Furthermore, the storage stability of the Ni SA/NC-based electrode was assessed after exposure to

Just Accepted

ambient conditions for one month (30 days). As shown in Fig. S31 in the ESM, it retains 94.38% and 93.02% of its initial peak currents for DA and HQ, respectively, confirming its favorable stability. The same

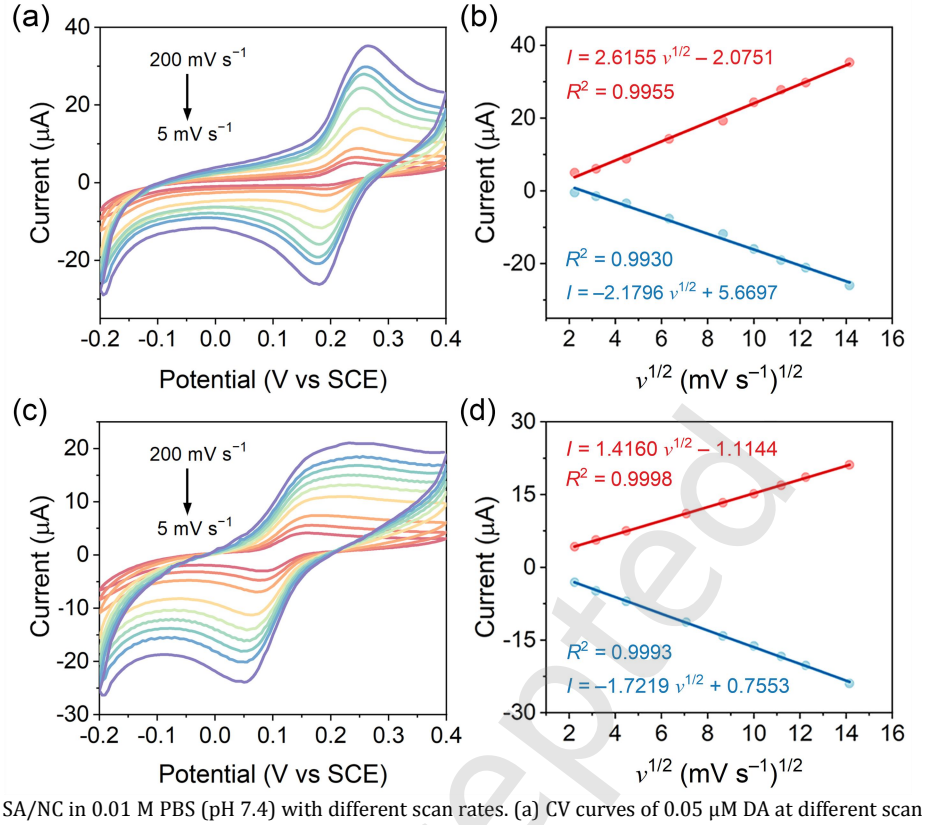


Figure 5 CV curves of Ni SA/NC in 0.01 M PBS (pH 7.4) with different scan rates. (a) CV curves of 0.05 μM DA at different scan rates. (b) Corresponding linear calibration curves of the peak currents versus the square root of scan rates for DA. (c) CV curves of 0.05 μM HQ at different scan rates. (d) Corresponding linear calibration curves of the peak currents versus the square root of scan rates for HQ.

electrode was tested for 28 consecutive days with current retention rates of 92.30% and 91.72% for DA and HQ, respectively, demonstrating reasonable long-term operational stability (Fig. S32 in the ESM). After 28 days of continuous testing, the modified material was scraped off for characterization (Figs. S33–S36 in the ESM). SEM, TEM, and HR-TEM showed no Ni nanoparticles, and the morphology and porous carbon framework remained the same as the as-prepared sample; XPS confirmed unchanged Ni chemical states; ICP-OES detected no Ni leaching in the electrolyte. Together, the post-use characterizations demonstrate that the Ni–N_4 active sites and the N-doped carbon support maintain chemical and structural integrity after long-term electrochemical operation. As shown in Table S5 in the ESM, recoveries of DA and HQ in human serum, urine, and lake water ranged from 95.2% to 104.6%, with RSDs below 5%. This confirms the excellent matrix tolerance and detection accuracy of the as-prepared Ni catalyst and its promise for practical applications. Taken together, these performance merits underscore the promising potential of Ni SA/NC as a reliable sensing material for practical analytical applications.

3.3 Mechanism investigation

To rationalize the exceptional activity of Ni SA/NC, we carried out density functional theory (DFT) calculations. Based on the electron microscopy and XAFS characterizations, a Ni–N_4 model was constructed to describe the Ni SA/NC catalyst (Fig. S37(a) in the ESM). The predominant Ni(111) face was used to represent the Ni NPs/NC counterpart (Fig. S37(b) in the ESM). Bader charge and charge density difference analyses of Ni–N_4 reveal that the Ni atoms transfer 0.95 *e* to the NC support (Figs. 6(a) and 6(b)). This manifests as strong electronic metal-support interactions, which can be further seen in the electron localization function (ELF) plot (Fig. 6(c)). As illustrated in Fig. 6(d), the *d*-band centers of Ni in Ni–N_4 and Ni(111) were −3.30 eV and −1.17 eV, respectively. Compared with Ni(111), the downshifted *d*-band center of Ni–N_4 is indicative of a more moderate adsorption behavior toward the analytes. As depicted in Fig. 6(e) and Figs. S38 and S39 in the ESM, the Ni–N_4 adsorbs DA and HQ with a lower affinity than those on Ni(111). This observation is in good agreement with the *d*-band center analysis. Figs. 6(f) and 6(h) show the calculated energy profiles of DA oxidation on Ni–N_4 and Ni(111) and corresponding configurations of various intermediates. The catalytic cycle begins with the adsorption of *OH at the Ni site of the Ni–N_4 moiety to generate the Ni–N_4/*OH intermediate. This species then reacts with DA through O–H bond activation to afford Ni–N_4/*OH + DA_H, which subsequently transforms into Ni–N_4. Upon release of H_2O, the Ni–N_4 moiety reverts to its initial state. The adsorption energy of Ni–N_4 and Ni(111) for *OH is 1.70 and −0.35 eV, respectively, indicating that *OH is more strongly adsorbed on Ni(111). As shown in Fig. S40 in the ESM, the Ni–O bond length on Ni(111) is 1.948 Å, shorter than that on Ni–N_4 (1.999 Å), indicating a stronger *OH adsorption on the Ni(111) surface. For the Ni–N_4 moiety, the formation of the Ni–N_4/*OH intermediate, with an energy change of 1.70 eV, constitutes the rate-determining step (RDS) for DA oxidation. In contrast, for Ni(111), the RDS shifts to the formation of the Ni(111)/*H_2O state, which suffers from a substantially

UNCorrected

higher energy change of 3.41 eV. As expected, a similar catalytic reaction route, shown in Fig. 6(g) and Fig. S41 in the ESM, is found for HQ adsorption on Ni–N_4 and Ni(111). The Ni–N_4 achieves a higher catalytic efficacy than Ni(111). The charge

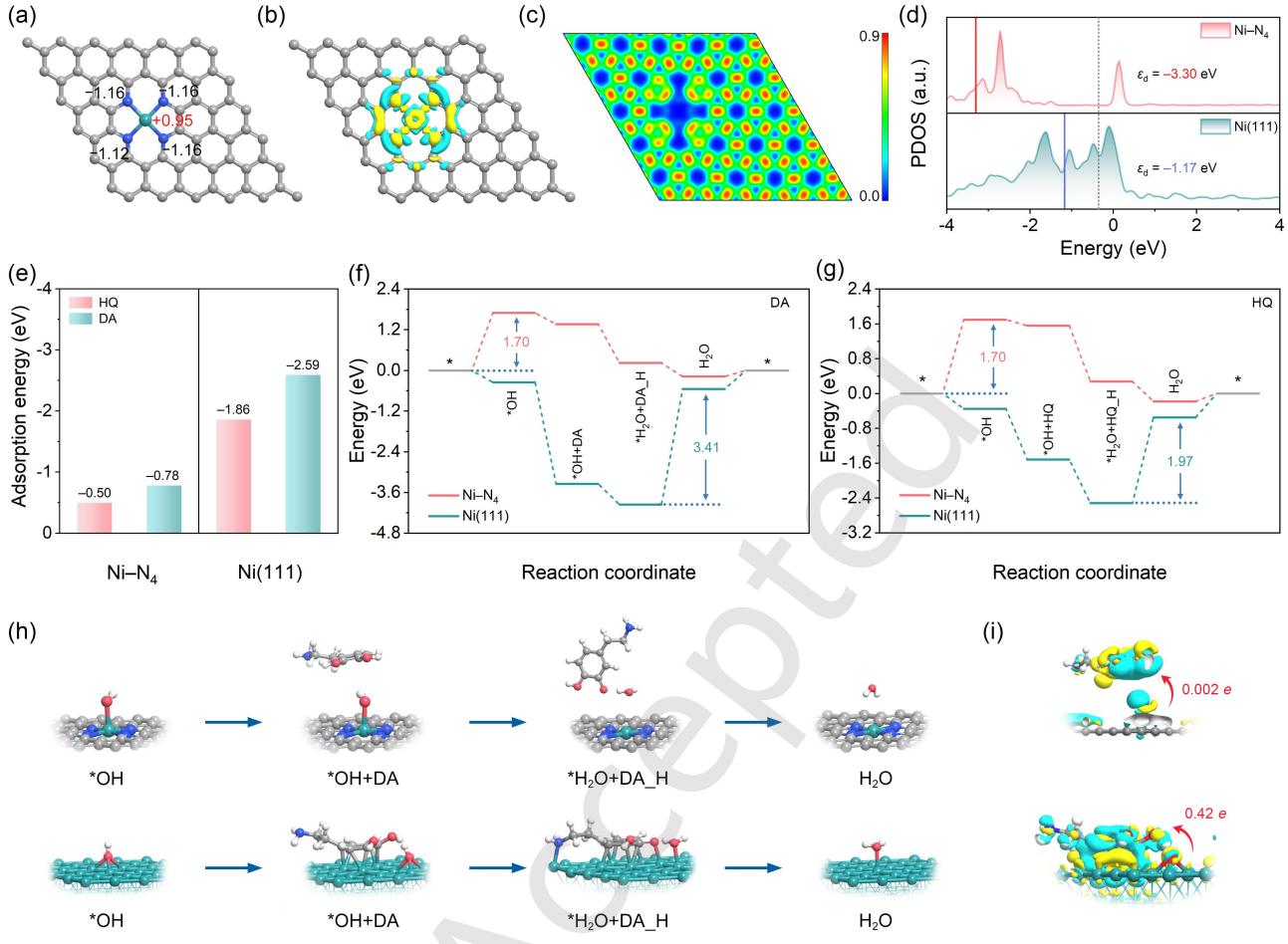


Figure 6 DFT calculations. (a) Bader charge, (b) charge density difference, and (c) ELF of Ni–N_4. (d) PDOS and *d*-band center of Ni–N_4 and Ni(111). (e) Calculated adsorption energies of HQ and DA on two models. Free energy diagrams of (f) DA and (g) HQ oxidation on Ni–N_4 and Ni(111), and (h) corresponding optimized intermediate configurations. (i) Charge density difference and Bader charge analysis of DA adsorbed on *OH pre-immobilized two models.

density difference and Bader charge analyses (Fig. 6(i) and Fig. S42 in the ESM) reveal that Ni(111) donates a substantially larger amount of charge (0.42 *e*) to DA compared with Ni–N_4 (0.002 *e*). This excessive charge transfer may hinder the effective activation of DA on Ni(111) in subsequent reaction steps. Additionally, the desorption of the final H_2O product on Ni–N_4 requires only 0.18 eV, significantly less than the 0.55 eV required on Ni(111). This low energy facilitates the rapid recovery of the Ni–N_4 site for the subsequent catalytic cycles. Unlike Xuan et al. [51], who used commercial residual carbon and acid-leaching controls for DA/uric acid sensing, we employ a bottom-up, highly reproducible Ni-MOF-74@PDA-derived Ni SAC with well-defined morphology and porosity for DA/HQ detection. Co SA/NC, Ni NPs/NC, and NC controls provide more rigorous mechanistic evidence, directly isolating the role of Ni–N_4 sites and revealing detailed electronic-structure modulation, stability, and anti-interference selectivity. Taken together, these findings demonstrate that Ni–N_4 exhibits superior catalytic activity toward DA oxidation compared to Ni(111).

4 Conclusions

In summary, we have developed a Ni single-atom catalyst (Ni SA/NC) by anchoring isolated Ni atoms onto an N-doped carbon support and have leveraged its unique electronic structure for the simultaneous detection of DA and HQ. Atomic-scale evidence confirms the Ni–N_4 coordination geometry, which is responsible for the remarkable sensing performance. Notably, the Ni SA/NC-modified electrode achieves low detection limits, wide linear ranges, and excellent reproducibility and storage stability. Electrochemical measurements reveal that the Ni–N_4 sites substantially reduce the interfacial charge-transfer resistance and accelerate the redox kinetics for both DA and HQ. DFT calculations further elucidate the underlying mechanism, showing that the atomically dispersed Ni–N_4 sites can modulate the *d*-band center to optimize intermediate adsorption, thereby enabling sensitive and simultaneous detection. This work provides a rational paradigm for designing single-atom catalysts for simultaneous electrochemical sensing of DA and HQ, with broad potential for early disease diagnosis.

Electronic Supplementary Material: Supplementary material (Figures S1–S42 and Tables S1–S7) is available in

Just Accepted

the online version of this article at https://doi.org/10.26599/NR.2026.94909307.

Data availability

All data needed to support the conclusions in the paper are presented in the manuscript and the Electronic Supplementary Material. Additional data related to this paper may be requested from the corresponding author upon request.

Acknowledgements

This work was supported by the National Natural Science Foundation of China (22679027), the Heilongjiang Young Science and Technology Talents Support Program (RC2025QN043), the Special Foundation for Fostering Talents in Basic Research of the Northeast Petroleum University (2024KQ01), and the Fundamental Research Funds for the Provincial Universities of Heilongjiang (2024GPL-02). The authors also acknowledge the Hefei Advanced Computing Center for providing high-performance computing resources. The authors gratefully thank beamline 1W1B of Beijing Synchrotron Radiation Facility (BSRF) in Beijing and Catalysis and Surface Science Endstation of BL11U beamline in the National Synchrotron Radiation Laboratory in Hefei for XAS measurements. The authors also acknowledge the Catalysis and Surface Science Endstation at beamline BL11U for support in UPS and SRPES measurements.

Declaration of competing interest

All the contributing authors report no conflict of interests in this work.

Author contribution statement

Y. Z.: Investigation, data curation, validation, formal analysis, writing – original draft. Y.-J. W.: Data curation, formal analysis, methodology. X. L. and Q. W.: Investigation, validation, formal analysis, visualization. J. H. H., Y. W. and R. W.: Data curation and software. H. H.: Investigation, data curation. Z. L.: Conceptualization, funding acquisition, project administration, supervision, writing – review & editing. All the authors have approved the final manuscript.

Use of AI statement

None.

References

[1] Srivastava, D. K.; Navratna, V.; Tosh, D. K.; Chinn, A.; Sk, M. F.; Tajkhorshid, E.; Jacobson, K. A.; Gouaux, E. Structure of the human dopamine transporter and mechanisms of inhibition. *Nature* **2024**, *632*, 672–677.

[2] Sawamoto, N.; Doi, D.; Nakanishi, E.; Sawamura, M.; Kikuchi, T.; Yamakado, H.; Taruno, Y.; Shima, A.; Fushimi, Y.; Okada, T. et al. Phase I/Ⅱ trial of iPS-cell-derived dopaminergic cells for Parkinson's disease. *Nature* **2025**, *641*, 971–977.

[3] Xue, Y.; Hassan, Q.; Noroozifar, M.; Sullan, R. M. A.; Kerman, K. Microfluidic flow injection analysis system for the electrochemical detection of dopamine using diazonium-grafted copper nanoparticles on multi-walled carbon nanotube-modified surfaces. *Talanta* **2024**, *266*, 125030.

[4] Miao, C.; Wang, Z.; Chen, K.; Li, C.; An, Z.; Li, Y.; Wang, H.; Li, L.; Zhao, G. Molecular oxygen cascade reduction to •OH via coplanar dual-electrocatalytic zone achieving electrolyte-free water purification. *Nat. Water* **2026**, *4*, 507–520.

[5] Irfan, M.; Shafeeq, A.; Siddiq, U.; Bashir, F.; Ahmad, T.; Athar, M.; Butt, M. T.; Ullah, S.; Mukhtar, A.; Hussien, M. et al. A mechanistic approach for toxicity and risk assessment of heavy metals, hydroquinone and microorganisms in cosmetic creams. *J. Hazard. Mater.* **2022**, *433*, 128806.

[6] DeCaprio, A. P. The toxicology of hydroquinone—relevance to occupational and environmental exposure. *Crit. Rev. Toxicol.* **1999**, *29*, 283–330.

[7] Yang, C.; Zhao, Y.; Dong, X.; Lu, S. Bimetallic cobalt–nickel supported on carbon fiber for electrochemical simultaneous determination of dopamine and hydroquinone. *Electrochem. Commun.* **2023**, *156*, 107597.

[8] Guiard, B. P.; Gotti, G. The high-precision liquid chromatography with electrochemical detection (HPLC-ECD) for monoamines neurotransmitters and their metabolites: a review. *Molecules* **2024**, *29*, 496.

[9] Lim, C.; Seah, D.; Vendrell, M. Chemical fluorophores for fluorescence lifetime imaging. *Chem. Soc. Rev.* **2026**, *55*, 1352–1370.

[10] Zhang, T.; Zhu, J.; Xie, M.; Meng, K.; Yao, G.; Pan, T.; Gao, M.; Cheng, H.; Lin, Y. Highly sensitive wearable sensor based on (001)‐orientated TiO_2 for real‐time electrochemical detection of dopamine, tyrosine, and paracetamol. *Small* **2024**, *20*, 2312238.

[11] Huang, H.; Chen, Y.; Chen, Z.; Chen, J.; Hu, Y.; Zhu, J.-J. Electrochemical sensor based on Ce-MOF/carbon nanotube composite for the simultaneous discrimination of hydroquinone and catechol. *J. Hazard. Mater.* **2021**, *416*, 125895.

[12] Lv, Y.; Zhu, K.; Li, J.; He, J.; Zhang, R.; Yang, Z.; Pan, P.; Li, H.; Cheng, Y.; Zheng, L. et al. Carbon material-based electrochemical immunosensor for influenza A virus detection. *Biochem. Eng. J.* **2026**, *230*, 110122.

[13] Leku, D. T.; Dessie, Y.; Tufa, L. T.; Ravikumar, C. R.; Yizengaw, M. B.; Bekele, E. T. Novel green synthesis of $ZnO/Co_3O_4/MnO_2$ ternary nanocomposites as high porous catalytic working electrode for the rapid electrochemical Pb^{2+} ions detection and quantification. *Inorg. Chem. Commun.* **2025**, *182*, 115630.

[14] Baker, C. O.; Huang, X.; Nelson, W.; Kaner, R. B. Polyaniline nanofibers: broadening applications for conducting polymers. *Chem. Soc. Rev.* **2017**, *46*, 1510–1525.

[15] Tian, Q.; Chen, S.; Yu, J.; Zhang, M.; Gao, N.; Yang, X.; Wang, C.; Duan, X.; Zang, L. Tunable construction of electrochemical sensors for chlorophenol detection. *J. Mater. Chem. C* **2022**, *10*, 10171–10195.

[16] Jin, H.; Guo, C.; Liu, X.; Liu, J.; Vasileff, A.; Jiao, Y.; Zheng, Y.; Qiao, S.-Z. Emerging two-dimensional nanomaterials for electrocatalysis. *Chem. Rev.* **2018**, *118*, 6337–6408.

[17] Yang, X.; Ma, L.; Wang, S.; Hu, X.; Li, B.; Li, W.; Wang, D.; Dai, Z. Electrochemiluminescence-based multiplex immunoassays for multianalyte bioanalysis: signal encoding strategies and analytical perspectives. *Electrochem. Commun.* **2026**, *186*, 108130.

[18] Yuan, H.; Chen, P.; Li, X.; Xu, X.; Qian, W.; Zhang, H.; Wang, Z.; Fu, H.; Wang, D.; He, D. Scalable fiber-skeleton-reinforced graphene-assembled films enabling wash-durable wearable heating. *Nano Res.* **2026**, *19*, 94908671.

[19] Wang, Z.; Wu, J.; Wei, W.; Gao, M.; Zhang, Y.-W.; Yu, Z. G.; Liang, Y. C.; Zhu, C. Pt single-atom electrocatalysts at Cu_2O nanowires for boosting electrochemical sensing toward glucose. *Chem. Eng. J.* **2024**, *495*, 153564.

[20] Paul, R.; Zhu, L.; Chen, H.; Qu, J.; Dai, L. Recent advances in carbon‐based metal‐free electrocatalysts. *Adv. Mater.* **2019**, *31*, 1806403.

[21] Lv, J.; Fratepietro, A.; Shao, M.; Fabiano, S.; Guo, X.; Facchetti, A. Synthesis and applications of conductive polymers. *Nat. Rev. Methods Primers* **2026**, *6*, 50.

[22] Gao, X.; Wei, H.; Ma, W.; Wu, W.; Ji, W.; Mao, J.; Yu, P.; Mao, L. Inflammation-free electrochemical in vivo sensing of dopamine with atomic-level engineered antioxidative single-atom catalyst. *Nat. Commun.* **2024**, *15*, 7915.

[23] Zhao, Y.; Wan, J.; Ling, C.; Wang, Y.; He, H.; Yang, N.; Wen, R.; Zhang, Q.; Gu, L.; Yang, B. et al. Acidic oxygen reduction by single-atom Fe catalysts on curved supports. *Nature* **2025**, *644*, 668–675.

[24] Gloag, L.; Somerville, S. V.; Gooding, J. J.; Tilley, R. D. Co-catalytic metal–support interactions in single-atom electrocatalysts. *Nat. Rev. Mater.* **2024**, *9*, 173–189.

[25] Ren, Y.; Yan, H.-M.; Zhang, L.; Liu, X.; Li, L.; Wang, Y.-G.; Li, J.;

Just Accepted

Zhang, T.; Wang, A. Fine-tuning the coordination structure and identifying Pt_1–O_v–Ce as the active site for selective hydrogenations over Pt_1/CeO_2 single-atom catalysts. *J. Am. Chem. Soc.* **2026**, *148*, 26039–26049.

[26] Wu, G.; Zelenay, P. Activity versus stability of atomically dispersed transition-metal electrocatalysts. *Nat. Rev. Mater.* **2024**, *9*, 643–656.

[27] Li, Z.; Liu, H.; Chen, Y.; Ji, S.; Lu, X.; Yang, W.; Wang, Y.; Horton, J. H.; Tang, Y.-J.; Tian, X. Modulation of d–d orbital hybridization *via* creating asymmetrical paired iron sites for the oxygen reduction reaction. *Energy Environ. Sci.* **2026**, *19*, 3891–3909.

[28] Wang, Y.; Ma, F.; Zhang, G.; Zhang, J.; Zhao, H.; Dong, Y.; Wang, D. Precise synthesis of dual atom sites for electrocatalysis. *Nano Res.* **2024**, *17*, 9397–9427.

[29] Gadipelli, S.; Guo, J.; Li, J.; Akbari, H.; Howard, C. A.; Zhang, H.; Skipper, N. T.; Barker, J.; Shearing, P. R.; Brett, D. J. L. Hydrogen generation promoted by single-atom-based thermochemical catalysts. *Nat. Rev. Chem.* **2026**, *10*, 538–557.

[30] Ji, S.; Wang, Y.-H.; Liu, H.; Lu, X.; Wang, Y.; Tian, X.; Zhao, Y.; Horton, J. H.; Li, Z. Site-specific synergy by heteronuclear microenvironment atomic editing for oxygen reduction reaction. *Nat. Commun.* **2025**, *16*, 11691.

[31] Shang, X.; Yu, B.; Min, X.-T.; Su, X.; Qiao, B.; Huang, Y. Regio‐ and site‐selective organic synthesis with single‐atom catalysts. *Angew. Chem. Int. Ed.* **2026**, *65*, e5513543.

[32] Li, Z.; Lu, X.; Guo, C.; Ji, S.; Liu, H.; Guo, C.; Lu, X.; Wang, C.; Yan, W.; Liu, B. et al. Solvent-free selective hydrogenation of nitroaromatics to azoxy compounds over Co single atoms decorated on Nb_2O_5 nanomeshes. *Nat. Commun.* **2024**, *15*, 3195.

[33] Wang, S.; Wang, L.; Zhou, X.; Fang, J.; Deng, C.; Wang, D. Design principles of single-atom catalysts anchored over porous materials for green catalysis and conversion. *Nano Res.* **2025**, *18*, 94907137.

[34] Zhang, H.; Fan, Y.; Guan, S.; Cui, W.-G.; Zhang, M.; Li, Z.; Dou, Y.; Yang, J.; Zhuang, Z.; Yuan, Z. et al. Research progress on Ti-based materials for MgH_2 hydrogen storage systems. *Comp. Funct. Mat.* **2025**, *1*, 20250201.

[35] Li, R.; Guo, W.; Zhu, Z.; Zhai, Y.; Wang, G.; Liu, Z.; Jiao, L.; Zhu, C.; Lu, X. Single-atom indium boosts electrochemical dopamine sensing. *Anal. Chem.* **2023**, *95*, 7195–7201.

[36] Yan, B.; Han, X.; Zhao, R.; Guo, Z.; Li, D.; Yan, Y.; Wang, D.; Yao, X. Simultaneous electrochemical and SPR detection of dopamine exocytosis from single cells and multiple cells using Au single atom modified carbon nanopipettes. *Anal. Chem.* **2025**, *97*, 23858–23867.

[37] Zhang, L.; Liu, R.; Tian, Y.; Wang, Y.; Bian, W. Review of single-atom nanozymes for detection of biomolecules, pollutants, microbes, and food additives. *ACS Appl. Nano Mater.* **2026**, *9*, 12166–12181.

[38] Wu, H.; Li, Y.-Z.; Li, Z.; Zhao, Z.; Li, X.; Guo, X.; Zhao, D.; Sui, Y.; Qi, J.; Xue, X. et al. MOF‐74 as a platform for metal node‐guided chloride storage mechanisms in anion‐based batteries. *Adv. Funct. Mater.* **2026**, *36*, e24152.

[39] Qian, C.; Xu, Y.; Wen, Y.; Zhang, J.; Wang, G.; Yuan, F.; Li, C.; Sun, Z. Cost-effective microwave-assisted synthesis of diatomite-supported MOF-74 for CO_2 capture toward potential net-negative emissions. *Chem. Eng. J.* **2026**, *544*, 179233.

[40] Xia, H.; Sun, M.; Yang, D.; Pang, R.; Zeng, Q.; Huang, L.; Huang, B.; Li, J.; Wang, E. Phosphorus/sulfur-modulated p-band center of pentagonal carbon for efficient oxygen reduction reaction. *J. Am. Chem. Soc.* **2025**, *147*, 41472–41480.

[41] Feng, X.; Chen, G.; Cui, Z.; Qin, R.; Jiao, W.; Huang, Z.; Shang, Z.; Ma, C.; Zheng, X.; Han, Y. et al. Engineering electronic structure of nitrogen‐carbon sites by sp^3‐hybridized carbon and incorporating chlorine to boost oxygen reduction activity. *Angew. Chem. Int. Ed.* **2024**, *136*, e202316314.

[42] Fan, Q.; Hou, P.; Choi, C.; Wu, T.-S.; Hong, S.; Li, F.; Soo, Y.-L.; Kang, P.; Jung, Y.; Sun, Z. Activation of Ni particles into single Ni–N atoms for efficient electrochemical reduction of CO_2. *Adv. Energy Mater.* **2020**, *10*, 1903068.

[43] Zhao, C.; Liu, Y.; Huo, F.; Guo, Z.; Lu, Y.; Sun, B.; Li, M.; Xu, H.; Zhang, M.; Fan, H. et al. Synergistic catalysts for lithium‐sulfur batteries: Ni single atom and MoC nanoclusters composites. *Angew. Chem. Int. Ed.* **2025**, *64*, e202502177.

[44] Ji, S.; Mou, Y.; Liu, H.; Lu, X.; Zhang, Y.; Guo, C.; Sun, K.; Liu, D.; Horton, J. H.; Wang, C. et al. Manipulating the electronic properties of an Fe single atom catalyst via secondary coordination sphere engineering to provide enhanced oxygen electrocatalytic activity in zinc‐air batteries. *Adv. Mater.* **2024**, *36*, 2410121.

[45] Lin, Z.; Yang, Y.; Li, M.; Huang, H.; Hu, W.; Cheng, L.; Yan, W.; Yu, Z.; Mao, K.; Xia, G. et al. Dual graphitic‐N doping in a six‐membered C‐ring of graphene‐analogous particles enables an efficient electrocatalyst for the hydrogen evolution reaction. *Angew. Chem. Int. Ed.* **2019**, *58*, 16973–16980.

[46] Pan, Y.; Chen, Y.; Wu, K.; Chen, Z.; Liu, S.; Cao, X.; Cheong, W.-C.; Meng, T.; Luo, J.; Zheng, L. et al. Regulating the coordination structure of single-atom Fe-N_xC_y catalytic sites for benzene oxidation. *Nat. Commun.* **2019**, *10*, 4290.

[47] Chen, Y.; Sun, X.; Biswas, S.; Xie, Y.; Wang, Y.; Hu, X. Integrating polythiophene derivates to PCN-222(Fe) for electrocatalytic sensing of L-dopa. *Biosens. Bioelectron.* **2019**, *141*, 111470.

[48] Ahmed, J.; Rahman, M. M.; Siddiquey, I. A.; Asiri, A. M.; Hasnat, M. A. Efficient hydroquinone sensor based on zinc, strontium and nickel based ternary metal oxide (TMO) composites by differential pulse voltammetry. *Sens. Actuators B* **2018**, *256*, 383–392.

[49] Costentin, C. Electrochemical approach to the mechanistic study of proton-coupled electron transfer. *Chem. Rev.* **2008**, *108*, 2145–2179.

[50] Liu, Y.; Hu, S.; Gan, N.; Yu, Z. Wearable patch biosensor through electrothermal film-stimulated sweat secretion for continuous sweat glucose analysis at rest. *Anal. Chem.* **2024**, *96*, 18510–18518.

[51] Qin, Z.; Tang, B.; Zhang, G.; Zhu, C.; Jiang, K.; Zhang, B.; Xuan, F. Single-atom Ni-N_4 for enhanced electrochemical sensing. *Nano Res.* **2024**, *17*, 7658−7664.

Just Accepted

Electronic Supplementary Material

Modulation of the electronic structure of a single-atom Ni catalyst for sensitive and simultaneous detection of dopamine and hydroquinone

Yanliang Zhai [1], Ying-Jun Wang [2], Xue Lu [1], Qian Wang [1], J. Hugh Horton [5], Yu Wang [4], Ruihan Wu [1], Heyong Huang [3] ✉, Zhijun Li [1] ✉

[1] State Key Laboratory of Continental Shale Oil, Joint International Research Laboratory of Advanced Chemical Catalytic Materials & Surface Science, College of Chemistry and Chemical Engineering, Northeast Petroleum University, Daqing 163318, China
[2] College of Chemical Engineering and Technology, Yantai Nanshan University, Yantai 265713, China
[3] School of Environment, Analysis and Testing Center, Nanjing Normal University, Nanjing 210023, China
[4] Jiangsu Collaborative Innovation Centre of Biomedical Functional Materials, School of Chemistry and Materials Science, Nanjing Normal University, Nanjing 210023, China
[5] Department of Chemistry, Queen's University, Kingston K7L 3N6, Canada

Supporting information to https://doi.org/10.26599/NR.2026.94909307

Just Accepted

Address correspondence to Zhijun Li, zhijun.li@queensu.ca; Heyong Huang, hhynjnu@126.com

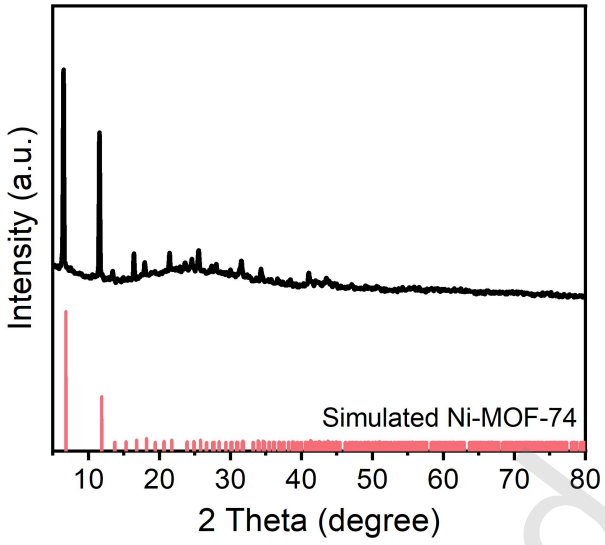


Figure S1 Experimental and simulated XRD patterns of Ni-MOF-74.

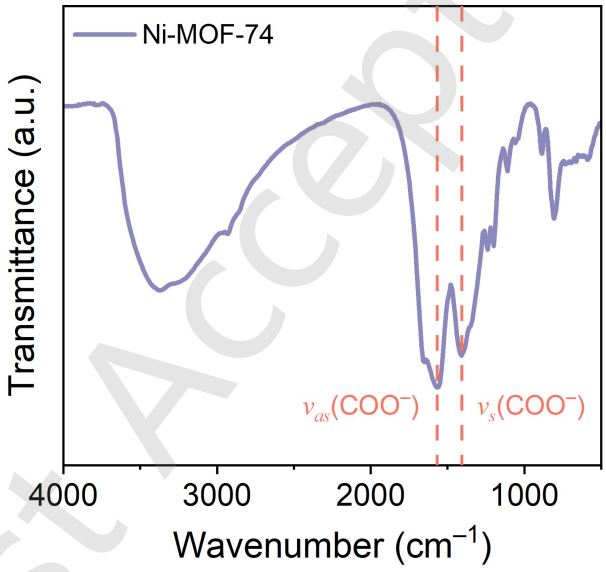


Figure S2 FT-IR spectrum of Ni-MOF-74.

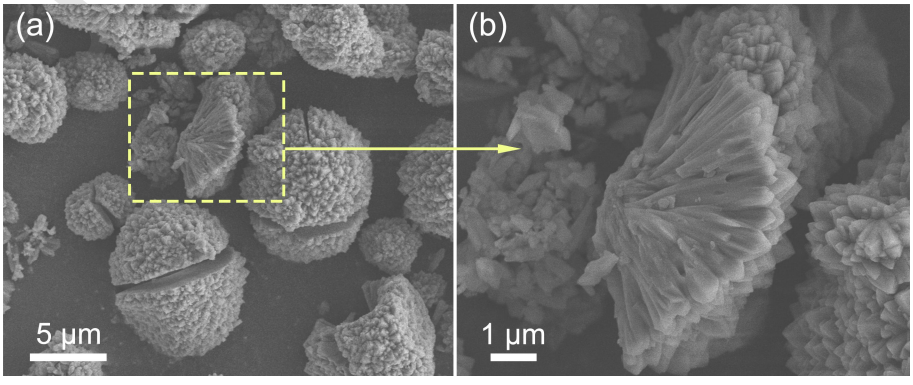


Figure S3 (a) SEM and (b) the enlarged SEM images of Ni-MOF-74.

Just Accepted

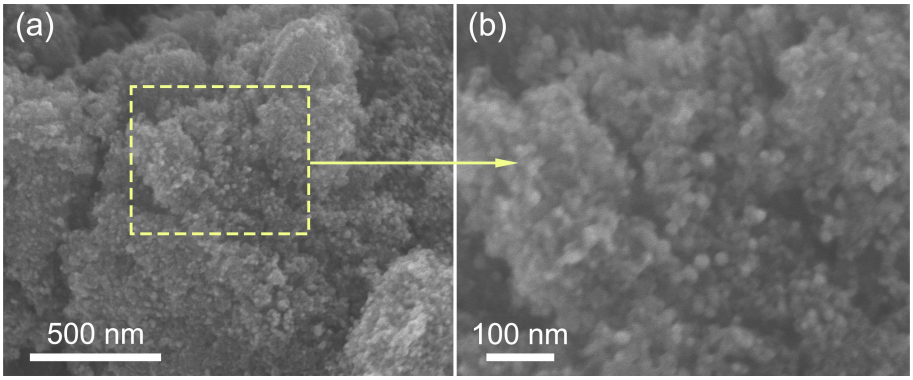


Figure S4 (a) SEM and (b) the enlarged SEM images of Ni NPs/NC.

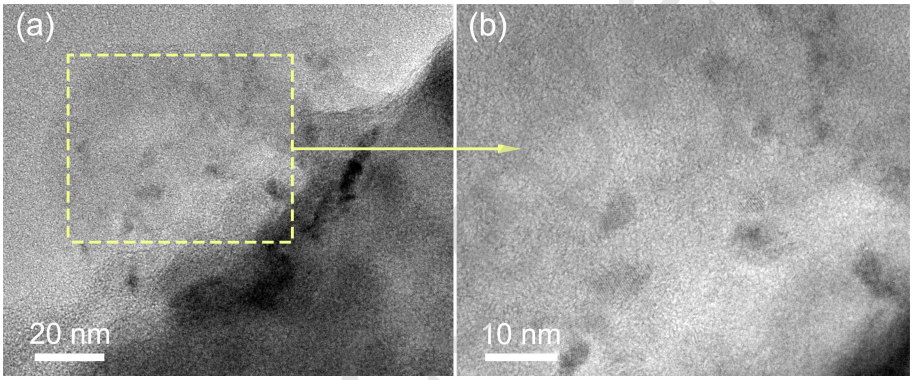


Figure S5 (a) TEM and (b) the enlarged TEM images of Ni NPs/NC.

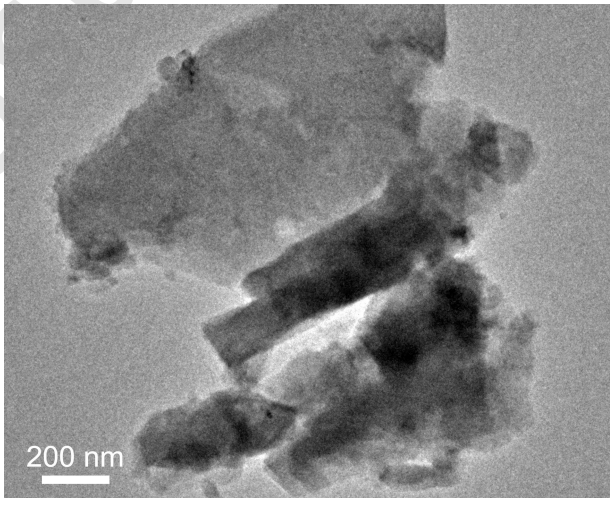


Figure S6 TEM image of NC.

Just Accepted

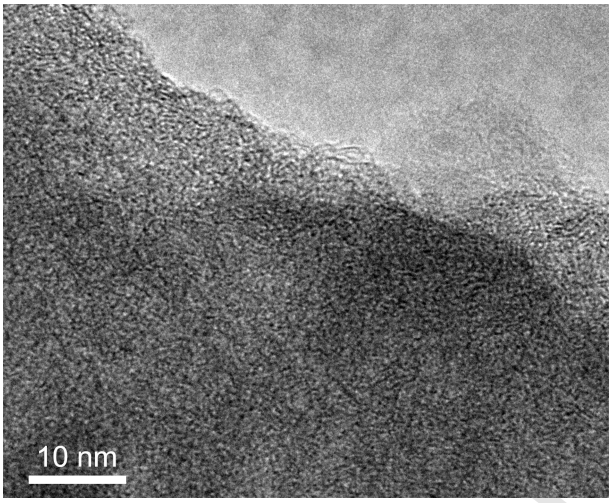


Figure S7 HR-TEM image of NC.

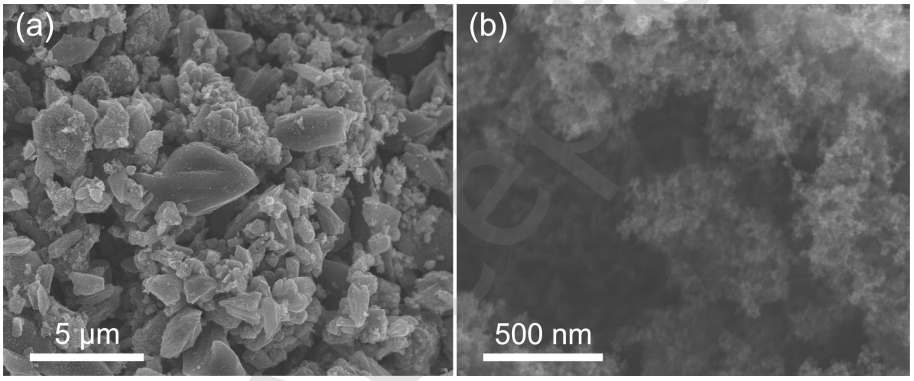


Figure S8 SEM image of Co SA/NC.

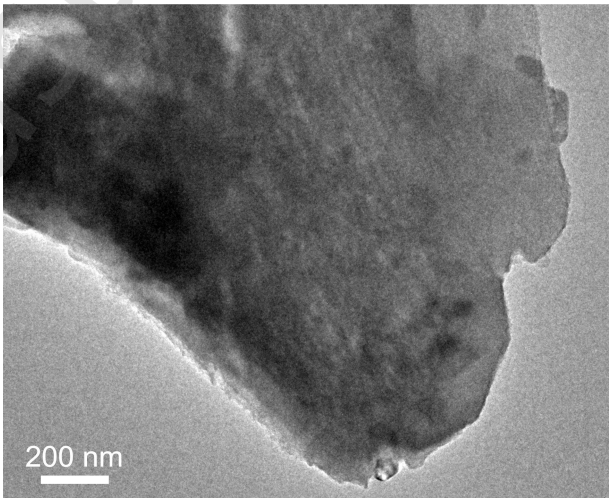


Figure S9 TEM image of Co SA/NC.

Just Accepted

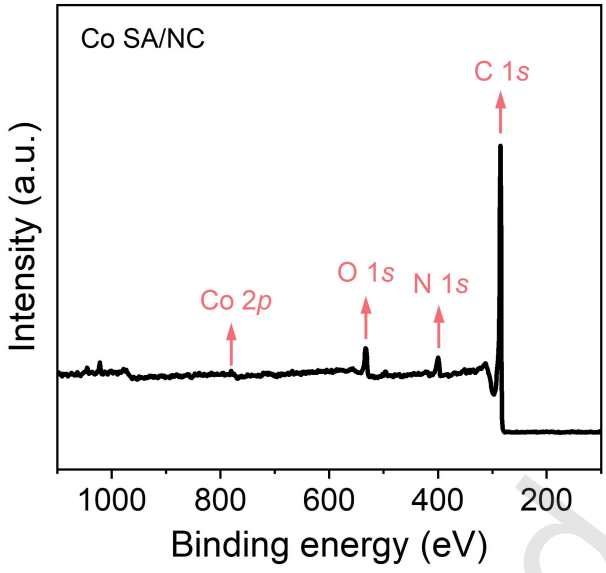


Figure S10 XPS survey spectrum of Co SA/NC.

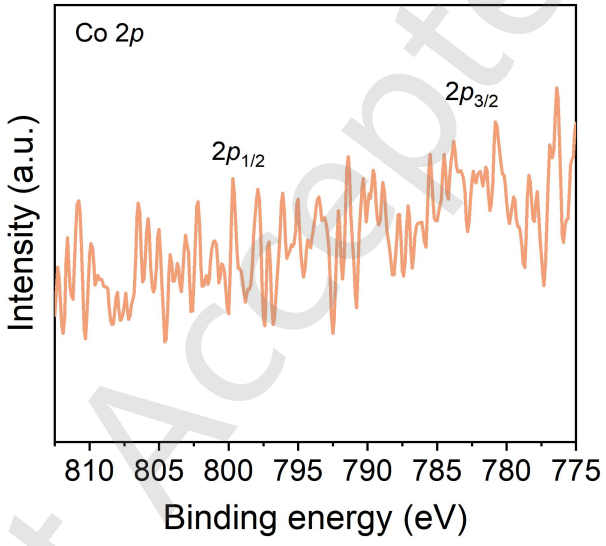


Figure S11 XPS Co 2*p* spectrum of Co SA/NC.

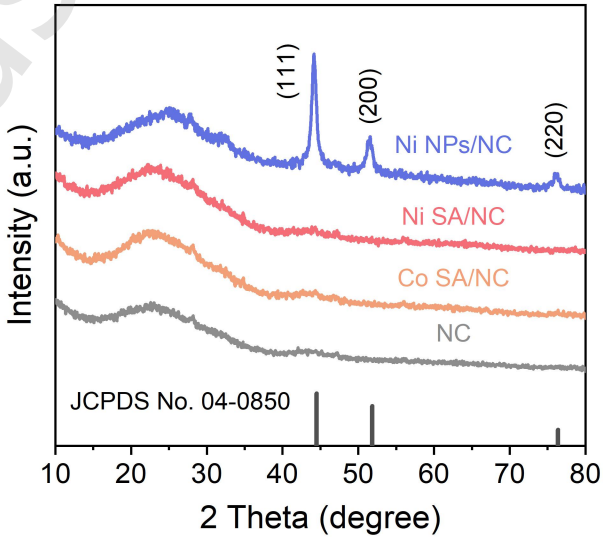


Figure S12 XRD patterns of Ni NPs/NC, Ni SA/NC, Co SA/NC, and NC.

Just Accepted

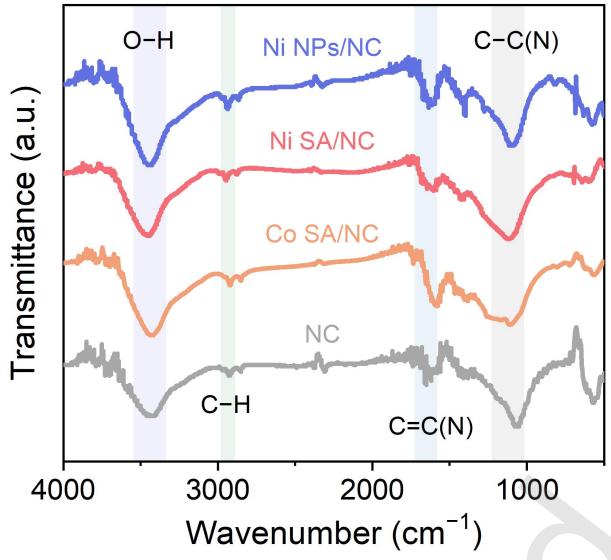


Figure S13 FT-IR spectra of Ni NPs/NC, Ni SA/NC, Co SA/NC, and NC.

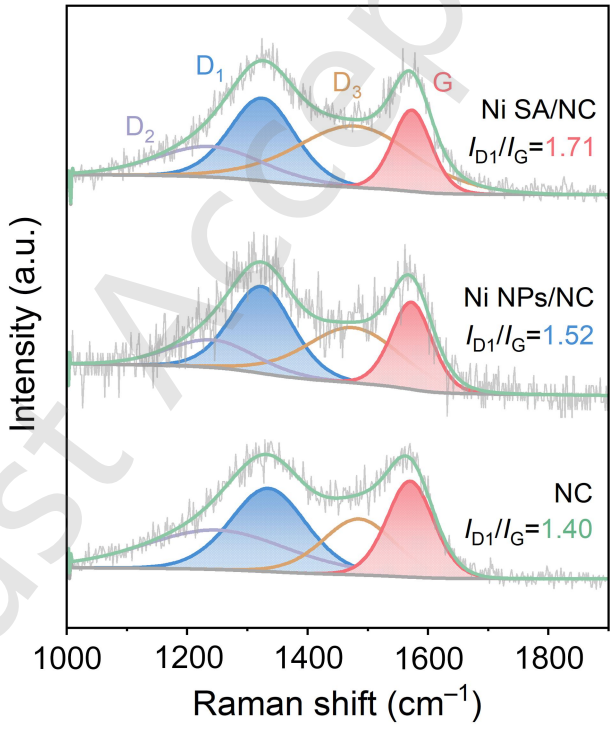


Figure S14 Raman spectra of Ni SA/NC, Ni NPs/NC, and NC.

Just Accepted

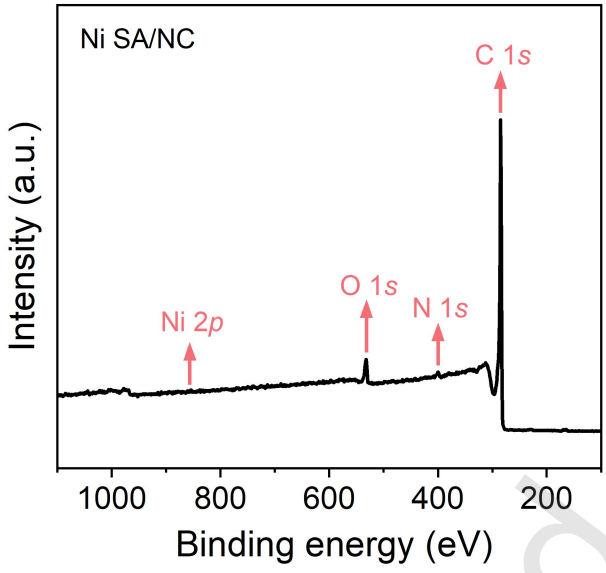


Figure S15 XPS survey spectrum of Ni SA/NC.

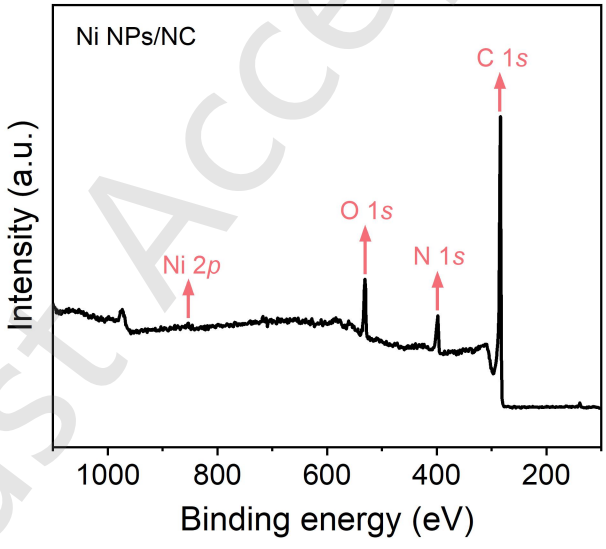


Figure S16 XPS survey spectrum of Ni NPs/NC.

Just Accepted

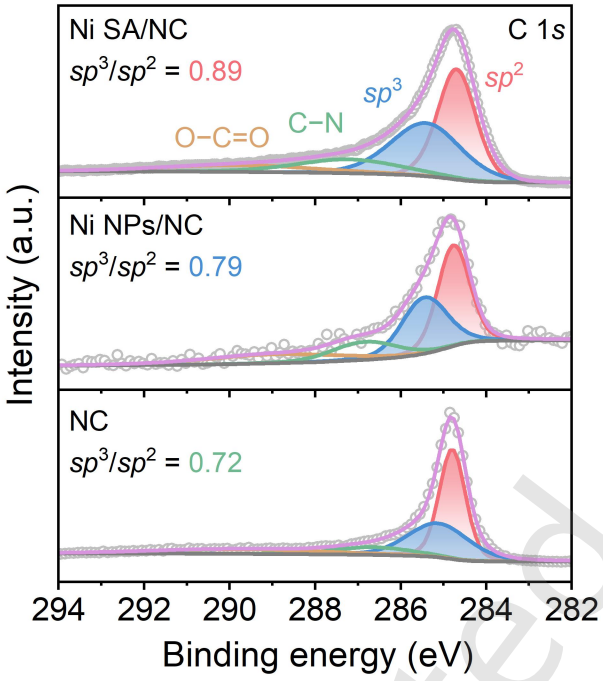


Figure S17 Comparison of SRPES C 1*s* spectra for Ni SA/NC, Ni NPs/NC, and NC.

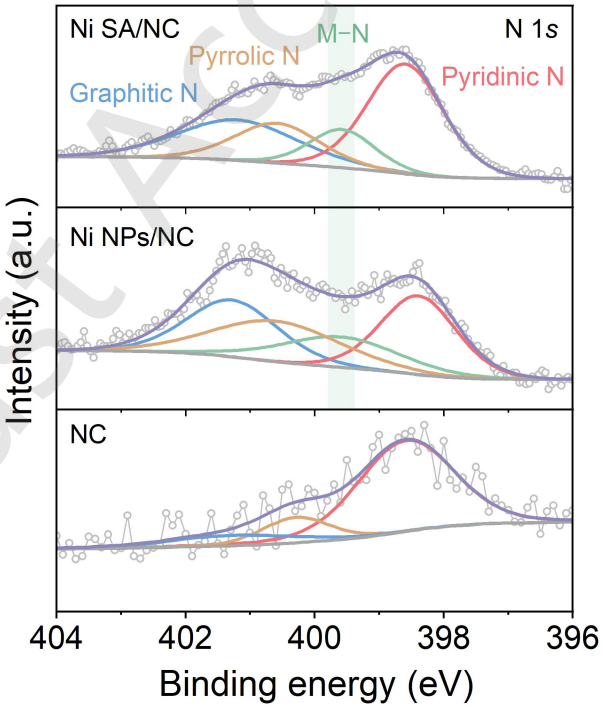


Figure S18 Comparison of SRPES N 1*s* spectra for Ni SA/NC, Ni NPs/NC, and NC.

Just Accepted

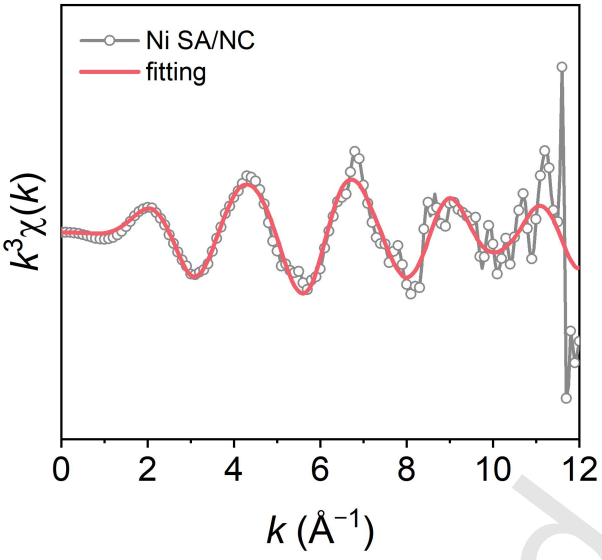


Figure S19 EXAFS fitting results in k space of Ni SA/NC.

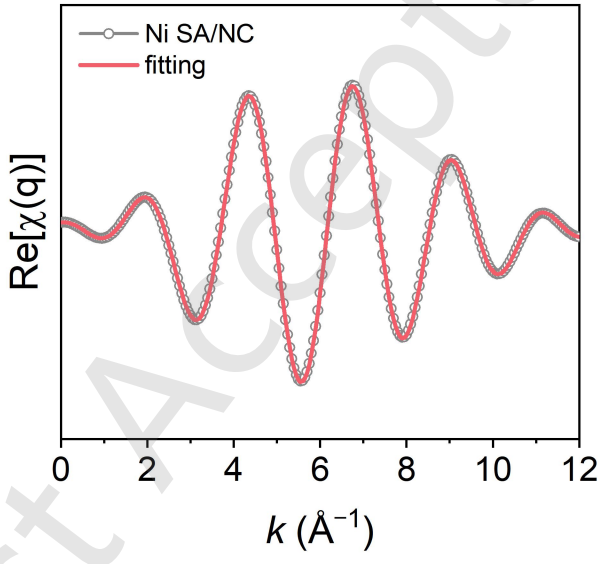


Figure S20 EXAFS fitting results in q space of Ni SA/NC.

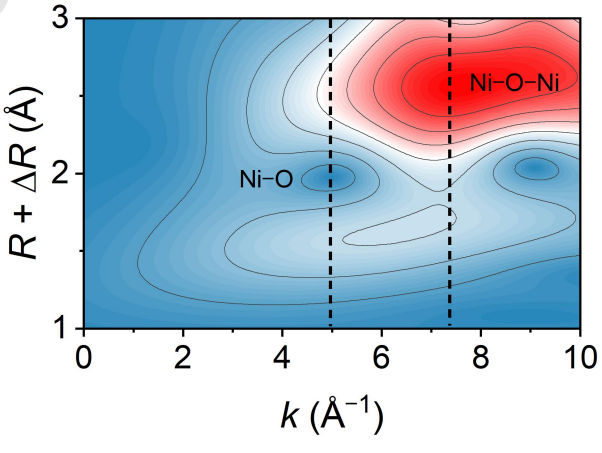


Figure S21 WT-EXAFS contour plot of NiO.

Just Accepted

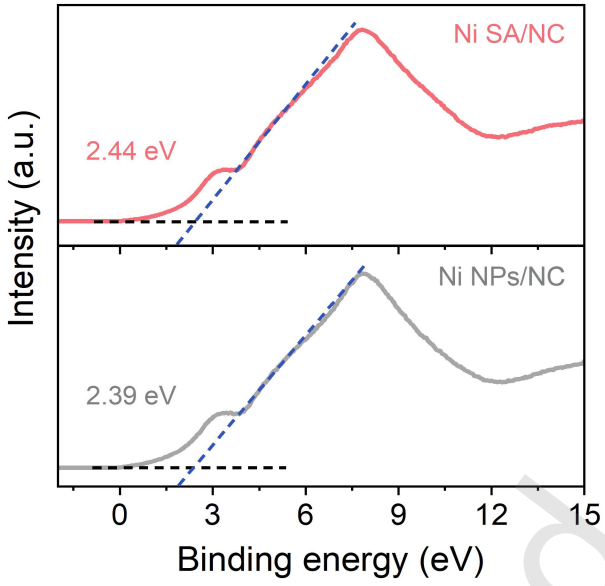


Figure S22 Valence band spectra of Ni SA/NC and Ni NPs/NC.

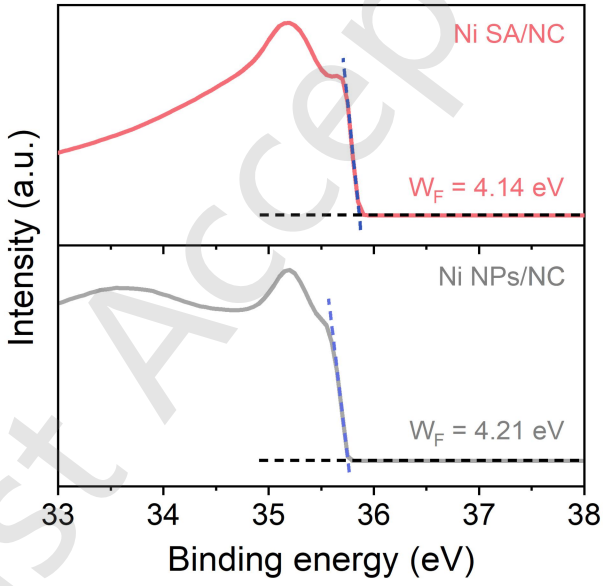


Figure S23 Secondary electron tail threshold spectra of Ni SA/NC and Ni NPs/NC.

Just Accepted

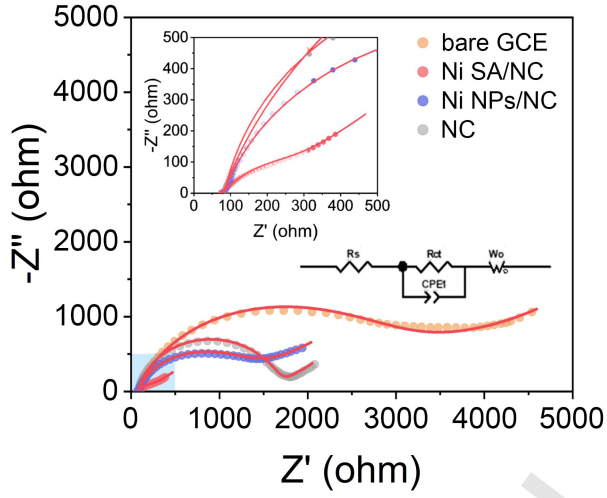


Figure S24 EIS plots of the bare GCE, Ni SA/NC, Ni NPs/NC, and NC.

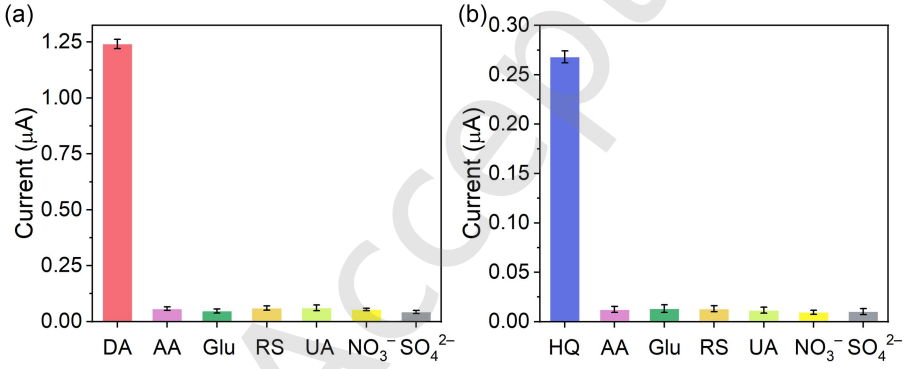


Figure S25 Selectivity of Ni SA/NC for detection of (a) DA and (b) HQ. The error bars show the standard deviations from three separate measurements.

Just Accepted

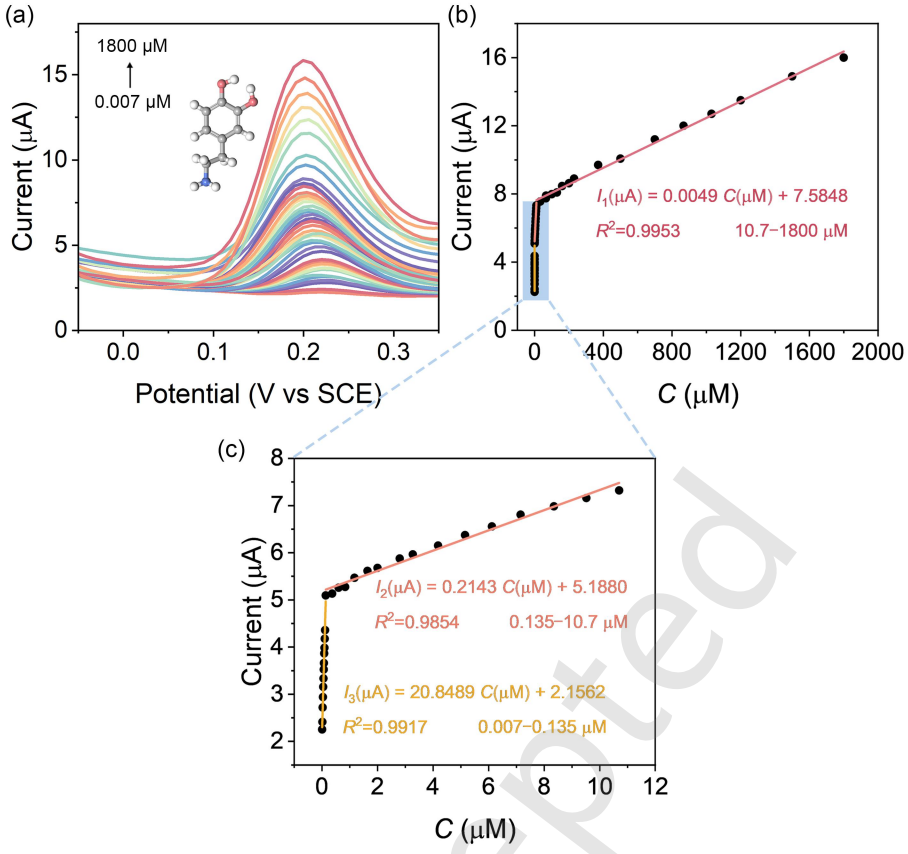


Figure S26 (a) DPV responses of different DA concentrations (0.007–1800 μM) on Ni SA/NC. (b, c) Corresponding calibration plots of the peak currents versus DA concentrations.

Just Accepted

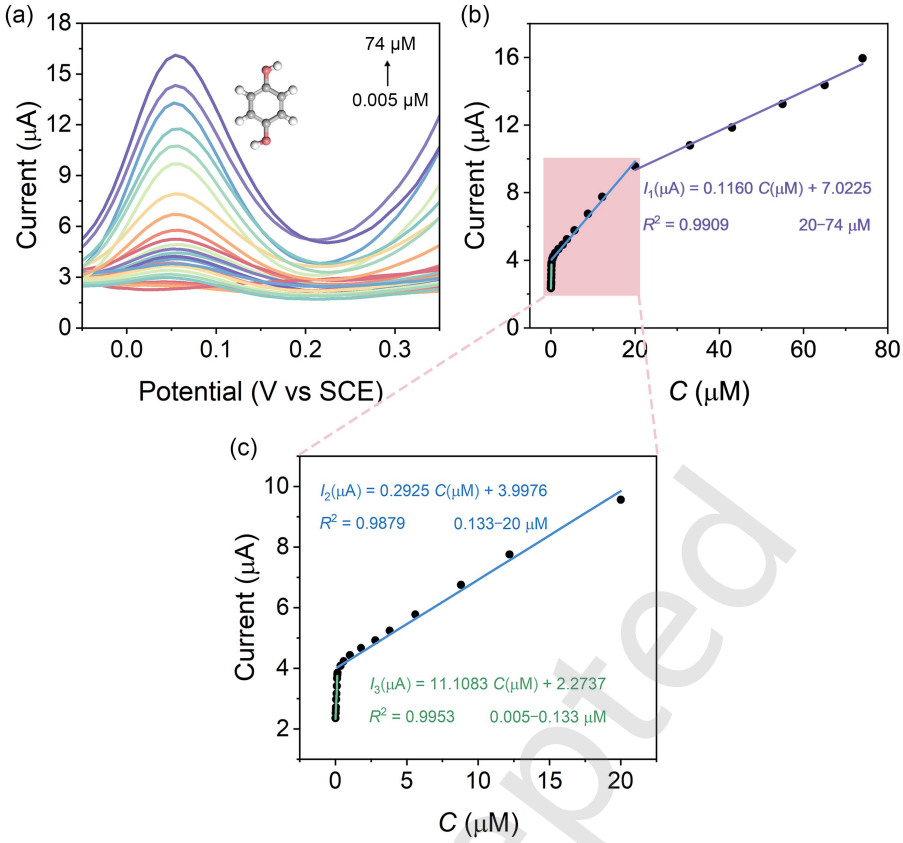


Figure S27 (a) DPV responses of different HQ concentrations (0.005–74 μM) on Ni SA/NC. (b, c) Corresponding calibration plots of the peak currents versus HQ concentrations.

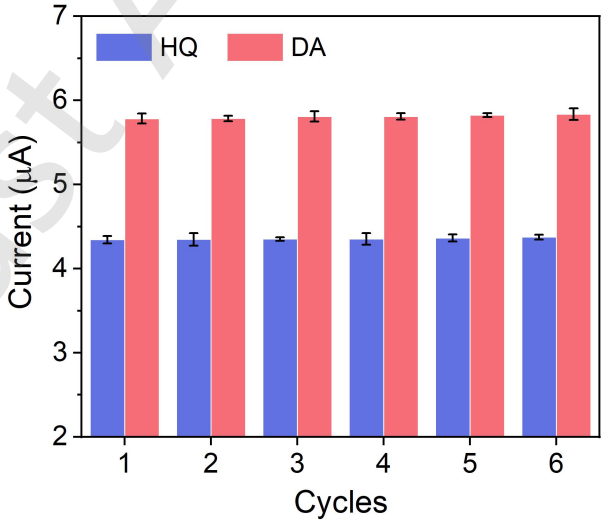


Figure S28 Reproducibility tests of Ni SA/NC in 0.01 M PBS (pH 7.4) with 0.05 μM DA and 0.05 μM HQ. The error bars show the standard deviations from three separate measurements.

Just Accepted

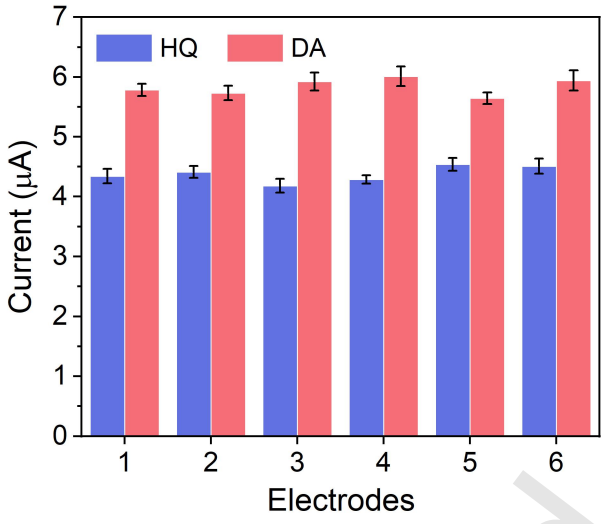


Figure S29 Batch-to-batch reproducibility of six Ni SA/NC-modified electrodes toward 0.05 μM DA and 0.05 μM HQ in 0.01 M PBS (pH 7.4).

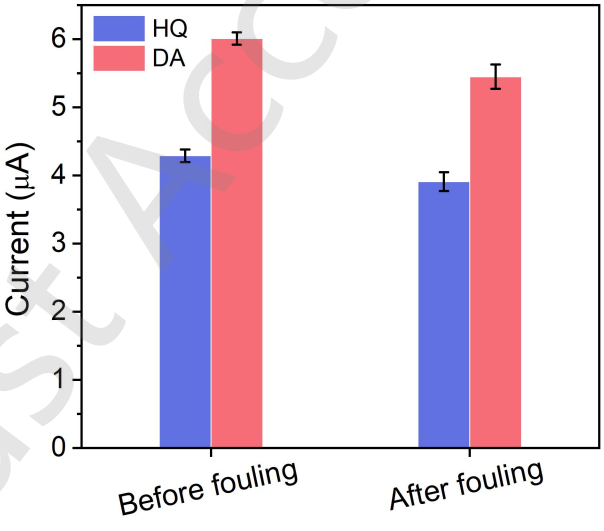


Figure S30 Anti-fouling testing of Ni SA/NC-modified electrode before and after immersion in 10% human serum for 4 h.

Just Accepted

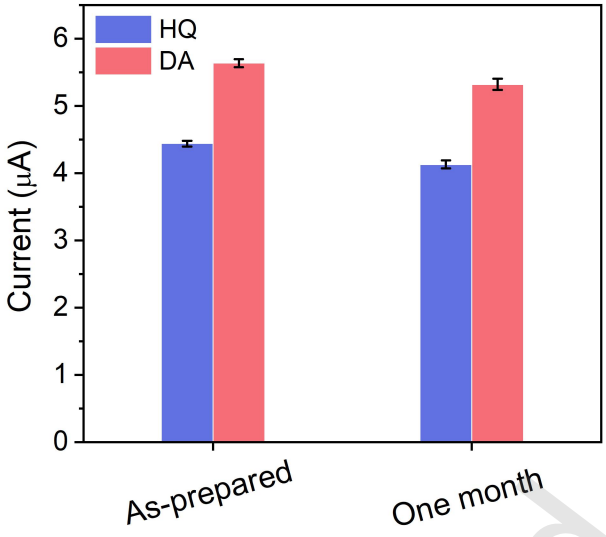


Figure S31 Storage stability testing of Ni SA/NC in 0.01 M PBS (pH 7.4) with 0.05 μM DA and 0.05 μM HQ.

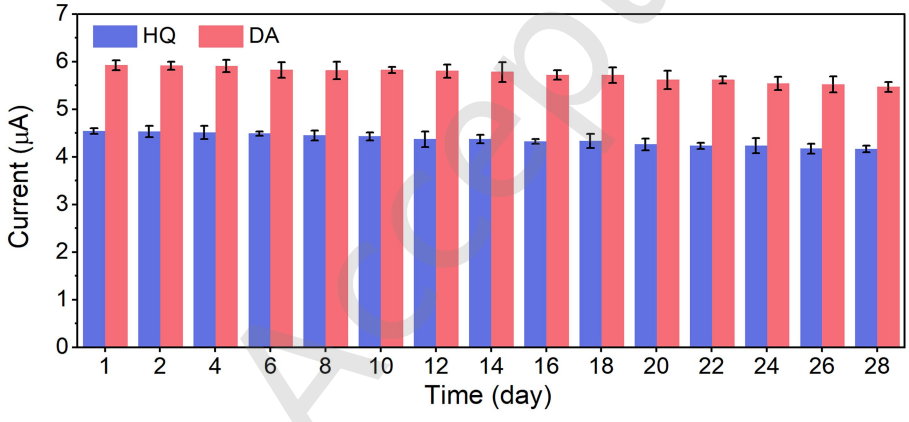


Figure S32 Long-term operational stability of Ni SA/NC-modified electrode toward 0.05 μM DA and 0.05 μM HQ in 0.01 M PBS (pH 7.4) over a 28-day testing period.

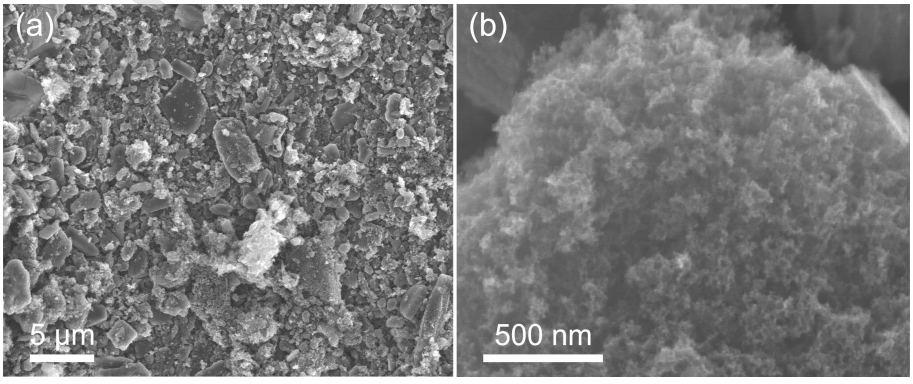


Figure S33 SEM images of Ni SA/NC after 28 days of electrochemical testing.

Just Accepted

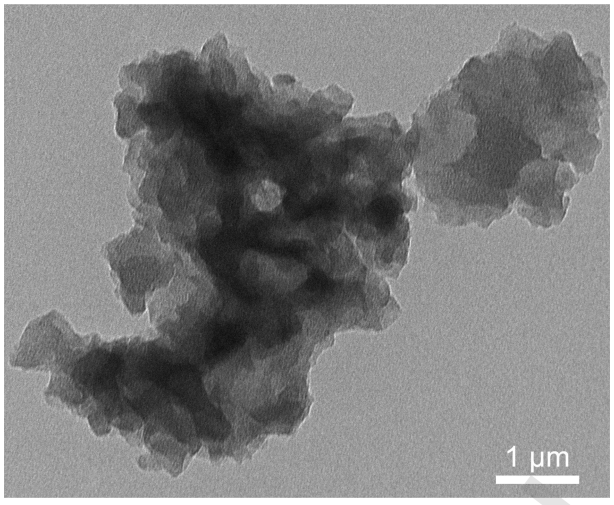


Figure S34 TEM image of Ni SA/NC after 28 days of electrochemical testing.

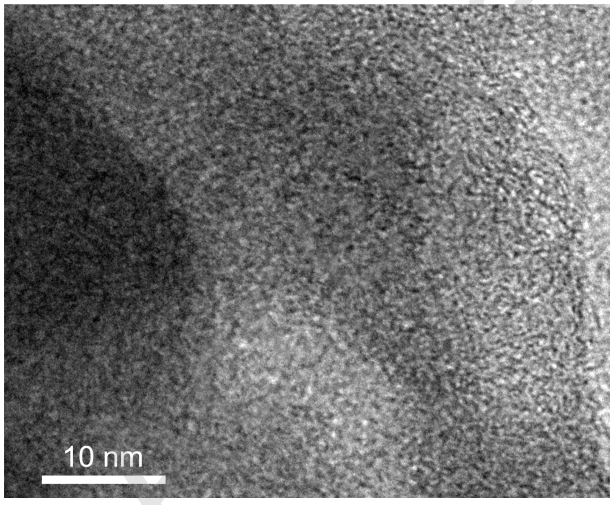


Figure S35 HR-TEM image of Ni SA/NC after 28 days of electrochemical testing.

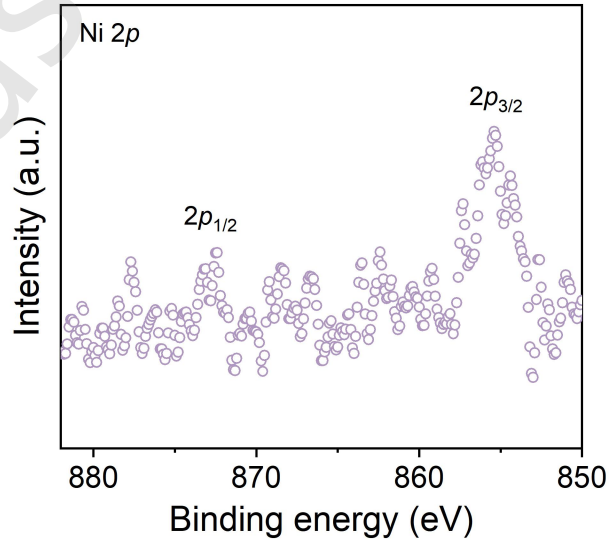


Figure S36 XPS Ni 2*p* spectrum of Ni SA/NC after 28 days of electrochemical testing.

Just Accepted

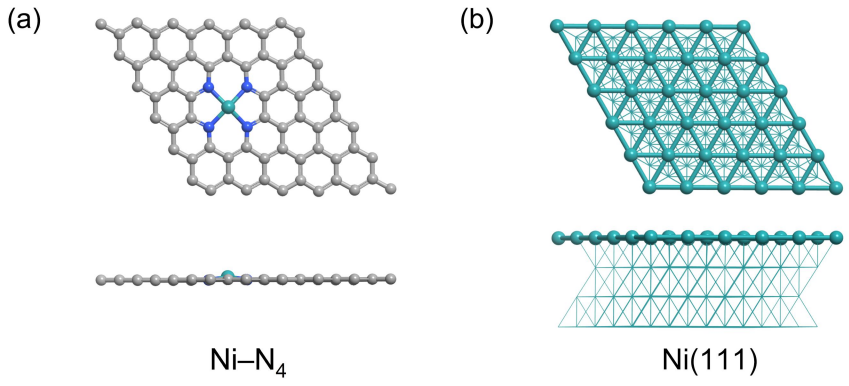


Figure S37 Structural models of (a) Ni–N_4 and (b) Ni(111).

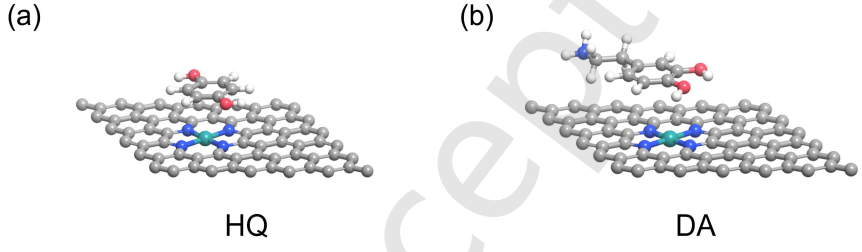


Figure S38 Side-view of the optimized structures of (a) HQ and (b) DA adsorbed on Ni–N_4 model.

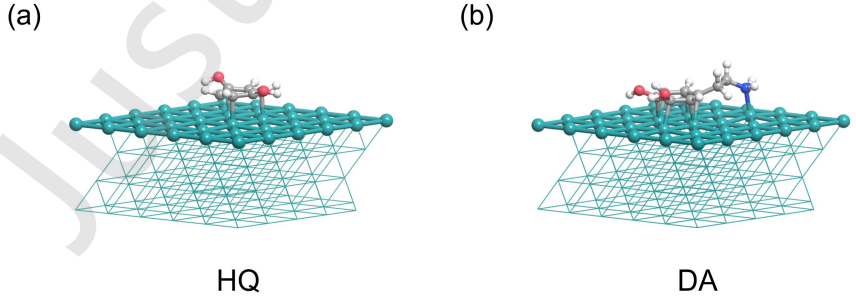


Figure S39 Side-view of the optimized structures of (a) HQ and (b) DA adsorbed on Ni(111) model.

Just Accepted

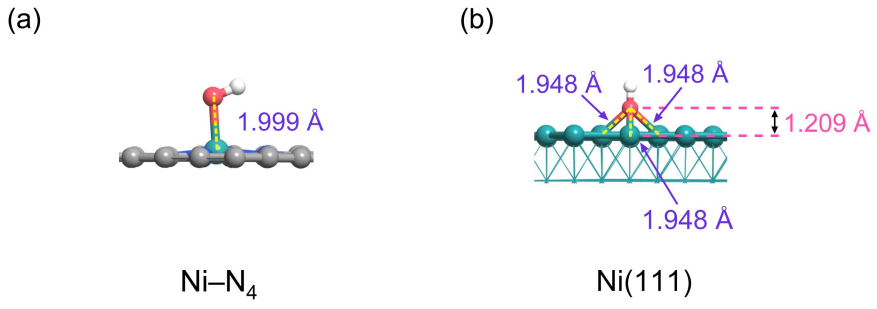


Figure S40 Bond lengths of Ni–O over *OH adsorbed on (a) Ni–N_4 and (b) Ni(111) models.

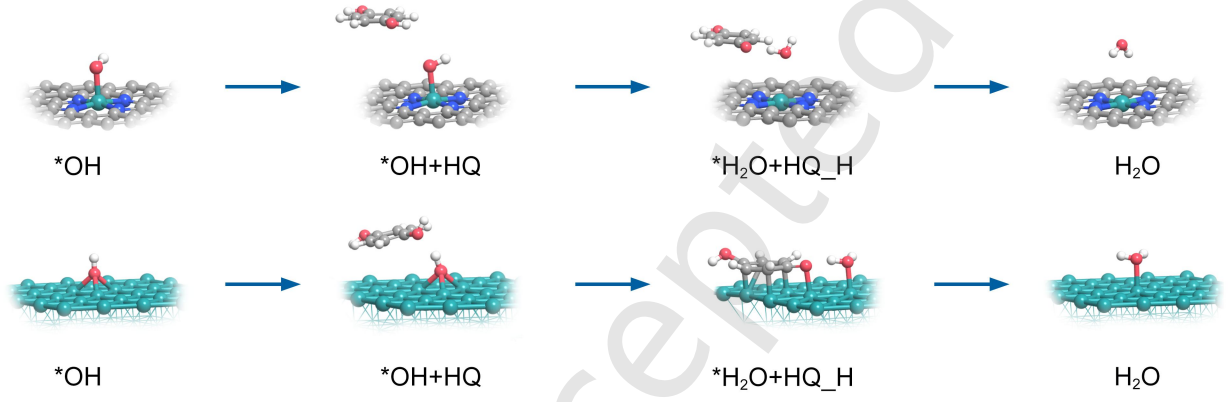


Figure S41 Reaction pathway (side-view) of the HQ oxidation on Ni–N_4 and Ni(111) and the corresponding intermediates configurations.

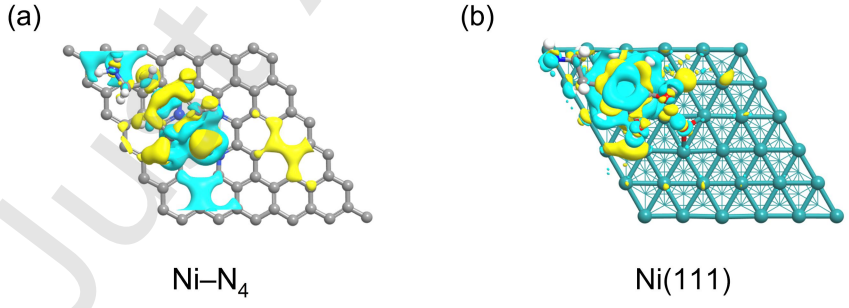


Figure S42 Top-view of charge density di erence and Bader charge analysis of DA adsorbed on *OH pre-immobilized (a) Ni–N_4 and (b) Ni(111) models.

Just Accepted

S3 Supplementary tables

Table S1 Relative ratios of the deconvoluted N species of Ni SA/NC, Ni NPs/NC, and NC from the SRPES N 1*s* spectra.

Sample	Pyridinic N (%)	Pyrrolic N (%)	Graphitic N (%)	Metal–N (%)
Ni SA/NC	44.37	17.43	24.89	13.31
Ni NPs/NC	30.39	24.46	27.18	17.98
NC	74.15	14.60	11.25	–

Table S2 Structural parameters extracted from the Ni K-edge EXAFS fitting. (S_0^2=0.86)

Sample	Scattering path	CN	*R* (Å)	σ^2 (10^{-3}Å^2)	ΔE_0 (eV)	*R* factor
Ni foil	Ni–Ni	12*	2.46	4.9	2.4	0.004
Ni SA/NC	Ni–N	3.8	1.98	4.4	3.5	0.009

S_0^2 is the amplitude reduction factor; CN is the coordination number; *R* is the interatomic distance (the bond length between Ni central atoms and surrounding coordination atoms); σ^2 is the Debye-Waller factor (a measure of thermal and static disorder in absorber-scatterer distances); ΔE_0 is the edge-energy shift (the difference between the zero kinetic energy value of the sample and that of the theoretical model). *R* factor is used to evaluate the goodness of the fitting.

* This value was fixed during EXAFS fitting, based on the known structure.

Error bounds that characterize the structural parameters obtained by EXAFS spectroscopy were estimated as $N \pm 20\%$; $R \pm 1\%$; $\sigma^2 \pm 20\%$; $\Delta E_0 \pm 20\%$.

Table S3 Current responses of Ni SA/NC, Ni NPs/NC, NC, and Co SA/NC for simultaneous detection of 0.05 μM DA and 0.05 μM HQ. (n=3)

Electrode materials	Target analyte	Average current (μA)	RSD (%)
Ni SA/NC	DA	5.64±0.19	3.37%
	HQ	4.44±0.20	4.50%
Ni NPs/NC	DA	3.05±0.15	4.92%
	HQ	2.67±0.10	3.75%
NC	DA	1.54±0.07	4.55%
	HQ	1.76±0.06	3.41%
Co SA/NC	DA	2.67±0.12	4.49%
	HQ	2.39±0.10	4.18%

Table S4 EIS fitting parameters of the bare GCE, Ni SA/NC, Ni NPs/NC, and NC.

Sample	R_s (Ω)	R_{ct} (Ω)	*Q* (F)	n
Ni SA/NC	68.7	128	7.106×10^{-4}	0.728
Ni NPs/NC	83.7	1228	4.771×10^{-5}	0.823
NC	80.3	1540	5.3581×10^{-6}	0.912
bare GCE	79.0	2501	2.8605×10^{-5}	0.810

Just Accepted

Table S5 Results for the detection of DA and HQ in real samples. (n=3)

Sample	Analyte	Added (μM)	Found (μM)	Recovery (%)	RSD (%)
Human serum	DA	0	ND	–	–
		0.05	0.0476	95.20	3.7
		5	4.82	96.40	1.9
		50	49.64	99.28	2.4
	HQ	0	ND	–	–
		0.05	0.0479	95.80	4.2
		5	4.91	98.20	3.4
		50	50.37	100.74	1.7
Human urine	DA	0	ND	–	–
		0.05	0.0518	103.60	4.8
		5	5.14	102.80	1.4
		50	49.76	99.52	2.3
	HQ	0	ND	–	–
		0.05	0.0483	96.60	3.9
		5	5.08	101.60	2.5
		50	49.42	98.84	1.8
Lake water	DA	0	ND	–	–
		0.05	0.0478	95.60	3.5
		5	5.04	100.80	2.7
		50	50.62	101.24	1.6
	HQ	0	ND	–	–
		0.05	0.0523	104.60	3.4
		5	4.91	98.20	2.5
		50	51.28	102.56	2.2

Just Accepted

Table S6 Comparison of as-prepared Ni SA/NC with other previously reported electrode materials for DA detection.

Electrode materials	Electrochemical method	LOD (μM)	Linear range (μM)	Area-normalized sensitivity ($\mu A \cdot \mu M^{-1} \cdot cm^{-2}$)	Loading (μg)	Reference
Ni SA/NC	DPV	0.0018	0.007−0.135 0.135−10.7 10.7−1800	165.48 1.67 0.039	25	This work
LIG/$Ni(NO_3)_2$+Urea	DPV	0.01786	0.25–16.44	–	–	*ACS Omega* **2026**, 11, 36141.
Cu_2CoS_4	DPV	0.003975	0.01–25	3.70	–	*Chem. Eng. Sci.* **2026**, 324, 123331.
AuNPs and MXene-SPE	DPV	1.11	1−500	–	2	*ACS Nano* **2025**, 19, 16980.
ZC31-$BTC_{700°C}$	DPV	0.04	0.1−500	0.0995	6	*Chem. Eng. J.* **2024**, 492, 152124.
CdS/MXene/g-C_3N_4	PEC	0.00048	0.001−100	–	–	*Adv. Funct. Mater.* **2024**, 34, 2410546.
TiO_2−CC	DPV	0.708	2−200 200−1000	1.390 0.318	–	*Small* **2024**, 20, 2312238.
E-AB	SWV	0.1	0.1−10	–	–	*Anal. Chem.* **2023**, 95, 6828.
D-PdMo	DPV	0.029	0.05−100	–	3	*Chem. Eng. J.* **2023**, 466, 143075.
N-GDY	i-t	0.46	1−550	0.374	41	*Chem. Eng. J.* **2023**, 464, 142629.
N−doped 4H−SiC	SWV	0.05	0.05−10.0	–	–	*Anal. Chem.* **2023**, 95, 4855.
AC-SGT	i-t	0.003	0.003−300	–	–	*ACS Sens.* **2023**, 8, 1211.
In_1−N−C	DPV	0.279	0−500	8.24	25	*Anal. Chem.* **2023**, 95, 7195.
ZnMOF/ITO	PEC	0.0177	0.03−10	–	30	*Biosens. Bioelectron.* **2022**, 211, 114369.
H−C/N@TiO_2	DPV	0.040	0.3–50	–	–	*J. Pharm. Anal.* **2022**, 12, 436.
NOCC-O	i-t	0.17	0.3−300	0.326	–	*Adv. Funct. Mater.* **2020**, 30, 1905361.

Just Accepted

Table S7 Comparison of as-prepared Ni SA/NC with other previously reported electrode materials for HQ detection.

Electrode materials	Electrochemical method	LOD (μM)	Linear range (μM)	Area-normalized sensitivity ($\mu A \cdot \mu M^{-1} \cdot cm^{-2}$)	Loading (μg)	Reference
Ni SA/NC	DPV	0.0017	0.005−0.133 0.133−20 20−74	88.17 2.30 0.95	25	This work
NiS_2-MoO_3@rGO	DPV	0.032	0.05−110	−	2	*Chem. Eng. J.* **2026**, 530, 173163.
30% CB/NFH	DPV	0.01	0.03−200	−	−	*Nanoscale* **2026**, 18, 13933.
$SrMnO_3$/g-C_3N_4	DPV	6.32	1−600	0.214	−	*J. Power Sources* **2025**, 640, 236761.
Co/HNC	DPV	0.023	1−100	−	10	*Anal. Chim. Acta* **2025**, 1357, 344074.
Mo_2C/C	DPV	0.13	0.5−1000	0.42	100	*Microchim. Acta* **2025**, 192, 350.
CaM@rGO	DPV	0.0086	0.05−105	−	2.5	*Sens. Actuators, B* **2024**, 420, 136481.
Mn_2SnO_4/*f*-CB	LSV	0.007	0.005–70.80	1.2903	60	*J. Ind. Eng. Chem.* **2024**, 133, 539.
CoP-NiCoP/GFs	DPV	0.256	1−101 101−601	−	11	*Nanoscale* **2023**, 15, 9823.
Lac-PB/PANI/CC	i-t	0.25	0.25−900	0.931	−	*Sens. Actuators, B* **2023**, 393, 134137.
CdS/SnS_2/CNTs	PEC	0.1	0.2−100	−	30	*J. Colloid Interface Sci.* **2023**, 643, 585.
N,S-$FeNi_3$/C	SWV	0.0135	0.05–70	1.2	5	*Microchim. Acta* **2023**, 190, 150.
***N*-rGO/CuO-ILCPE**	DPV	0.25	1.0−600.0	−	−	*Chemosphere* **2022**, 302, 134712.
Zn@ZnO	CV	0.10443	10−90	0.5673	20	*Environ. Res.* **2022**, 204, 112340.
Mo SAs/NPO-C	DPV	0.005	0.08−200	−	10	*J. Hazard. Mater.* **2022**, 437, 129327.
Ce-MOF (TV)/CNTs	DPV	5.3	10−100	−	−	*J. Hazard. Mater.* **2021**, 416, 125895.

Just Accepted

References

[1] Lejaeghere, K.; Bihlmayer, G.; Björkman, T.; Blaha, P.; Blügel, S.; Blum, V.; Caliste, D.; Castelli, I. E.; Clark, S. J.; Dal Corso, A. et al. Reproducibility in density functional theory calculations of solids. *Science* **2016**, *351*, aad3000.

[2] Devi, R.; Singh, B.; Canepa, P.; Sai Gautam, G. Effect of exchange-correlation functionals on the estimation of migration barriers in battery materials. *npj Comput. Mater.* **2022**, *8*, 160.

[3] Goerigk, L.; Grimme, S. A thorough benchmark of density functional methods for general main group thermochemistry, kinetics, and noncovalent interactions. *Phys. Chem. Chem. Phys.* **2011**, *13*, 6670.

Just Accepted